

Thermodynamic Characterizations of Singular Bayesian Models: Specific Heat, Susceptibility, and Entropy Flow in Posterior Geometry

Sean Plummer

Independent Researcher
snplmmr@gmail.com

December 29, 2025

Abstract

Singular learning theory (SLT) [Watanabe, 2009, 2018] provides a rigorous asymptotic framework for Bayesian models with non-identifiable parameterizations, yet the statistical meaning of its second-order invariant, the *singular fluctuation*, has remained unclear. In this work, we show that singular fluctuation admits a precise and natural interpretation as a *specific heat*: the second derivative of the Bayesian free energy with respect to temperature. Equivalently, it measures the posterior variance of the log-likelihood observable under the tempered Gibbs posterior. We further introduce a collection of related thermodynamic quantities, including entropy flow, prior susceptibility, and cross-susceptibility, that together provide a detailed geometric diagnosis of singular posterior structure. Through extensive numerical experiments spanning discrete symmetries, boundary singularities, continuous gauge freedoms, and piecewise (ReLU) models, we demonstrate that these thermodynamic signatures cleanly distinguish singularity types, exhibit stable finite-sample behavior, and reveal phase-transition-like phenomena as temperature varies. We also show empirically that the widely used WAIC estimator [Watanabe, 2010, 2013] is exactly twice the thermodynamic specific heat at unit temperature, clarifying its robustness in singular models. Our results establish a concrete bridge between singular learning theory and statistical mechanics, providing both theoretical insight and practical diagnostics for modern Bayesian models.

1 Introduction

Modern Bayesian models are increasingly *singular*, their parameterizations are non-identifiable, their Fisher information matrices are degenerate, and classical asymptotic theory breaks down. Mixture models, latent variable models, matrix factorizations, and neural networks all exhibit singularities arising from symmetries, boundaries, or piecewise-defined likelihoods [Watanabe, 2009, Amari et al., 1995, Neal, 1996]. In these settings, standard tools such as the Bernstein–von Mises theorem fail [Kleijn and Van der Vaart, 2012], and learning behavior is governed by subtler geometric and statistical phenomena [Watanabe, 2009].

Singular Learning Theory (SLT) [Watanabe, 2009, 2018] provides a rigorous asymptotic framework for such models. In SLT, the Bayesian free energy admits an expansion of the form

$$F_n = -nS + \lambda \log n - (m-1) \log \log n + O(1),$$

where the real log canonical threshold (RLCT) λ governs the leading learning rate and m is the multiplicity of the RLCT [Watanabe, 2009, 2018]. In contrast to λ (and m), which control the marginal-likelihood asymptotics, ν controls second-order *fluctuation* behavior through log-likelihood variance and related response functions. While the RLCT λ admits a clear geometric interpretation as an effective dimensionality near singular strata, no comparable geometric or physical interpretation has been given for the singular fluctuation ν , which is introduced through functional variance identities and equations of state [Watanabe, 2018, Chapter 7].

This paper revisits singular learning theory through the lens of statistical mechanics. By introducing a finite-temperature Gibbs posterior and studying derivatives of the Bayesian free energy, we show that singular fluctuation admits a precise and natural interpretation as the specific heat of the Bayesian posterior. From this perspective, ν measures the sensitivity of the free energy to temperature perturbations, or equivalently, the magnitude of posterior fluctuations of the log-likelihood observable.

Viewing Bayesian inference as a thermodynamic system does more than reinterpret a single constant. It opens the door to a family of response functions, such as specific heat, susceptibilities, and entropy flows, which together provide a detailed structural description of posterior behavior in singular models. These quantities diagnose not only how much uncertainty remains, but where it concentrates: along symmetry orbits, near boundaries, or across discrete active sets.

1.1 Motivation

Several empirical and theoretical puzzles motivate this work. First, in singular models, posterior uncertainty can persist even as predictive performance improves. Generalization error may shrink while the posterior continues to spread along non-identifiable directions. This phenomenon is invisible to local curvature diagnostics but plays a central role in model selection, uncertainty quantification, and learning dynamics. Second, many quantities used in practice, such as WAIC, are known to behave well in singular models, yet their deeper meaning is often obscured. Why does WAIC continue to work when effective dimension is ill-defined? What exactly is it measuring when the posterior is multimodal or supported on a manifold? Third, thermodynamic analogies are often invoked informally in Bayesian inference and machine learning, but rarely made precise. While free energy and temperature are widely used metaphors, few works identify concrete response functions or connect them directly to the invariants of singular learning theory. Our goal is to resolve these issues by developing a coherent thermodynamic framework for singular Bayesian models that is mathematically grounded, statistically interpretable, and empirically operational.

1.2 Contributions

The main contributions of this paper are as follows:

- We show that Watanabe’s singular fluctuation ν is exactly a *specific heat*: a second derivative of the Bayesian free energy that measures posterior fluctuations of the log-likelihood observable.
- We introduce additional thermodynamic response functions for singular models, including prior susceptibility, cross-susceptibility, entropy flow, and active-set entropy, each capturing a distinct aspect of posterior geometry.
- We empirically study four canonical singularities, including discrete symmetry, boundary singularity, continuous gauge symmetry, and piecewise (ReLU) singularity, and demonstrate how thermodynamic quantities reveal their distinct geometric fingerprints.

- We provide practical Monte Carlo estimators for all quantities and validate their behavior through extensive numerical experiments, including finite-sample scaling and estimator comparisons.
- We clarify the relationship between singular fluctuation and WAIC, showing empirically that WAIC is precisely twice the thermodynamic specific heat at $\beta = 1$.

Together, these results elevate singular fluctuation from an abstract asymptotic constant to a finite-temperature diagnostic of posterior geometry, connecting singular learning theory with statistical physics in a concrete and operational way.

2 Background and Related Work

This section provides a concise overview of the mathematical and statistical foundations underlying our thermodynamic characterization of singular learning. We briefly outline the core concepts from singular learning theory, connect them with classical Bayesian and thermodynamic formulations, and position our contribution relative to prior work in statistics, machine learning, and statistical physics.

2.1 Singular Learning Theory and Its Asymptotics

Many modern statistical models, including mixture models, latent variable models, factorization models, and neural networks, are *singular*: their Fisher information matrices are degenerate and the parameterization fails to be locally identifiable. Classical regular asymptotic theory (e.g. Bernstein–von Mises) therefore does not apply.

Watanabe’s *singular learning theory* (SLT) [Watanabe, 2009, 2018] provides a resolution by analyzing the geometry of the *Kullback–Leibler divergence* through tools from algebraic geometry. Two quantities govern the asymptotic expansion of the Bayesian free energy:

$$F_n = -nS + \lambda \log n - \nu + o(1),$$

where λ is the *real log canonical threshold* (RLCT) and ν is the *singular fluctuation*. The RLCT determines the learning rate and generalization error, while ν appears in WAIC, Bayesian model selection criteria, and the constant term of the free-energy expansion.

Although the RLCT has a well-understood geometric interpretation (measuring the local “dimension” of the singularity), the *statistical meaning of ν has been unclear*. Watanabe explicitly notes: “*The statistical interpretation of singular fluctuation remains an open question.*”

Our work addresses this gap by showing that ν admits a natural interpretation as a *specific heat* of the posterior, derived from second derivatives of the Gibbs free energy, and by introducing a suite of associated response functions.

2.2 Gibbs Posteriors and Thermodynamic Analogies

Bayesian posteriors can be written in Gibbs form [Catoni, 2004, Alquier et al., 2016, Grünwald, 2012],

$$p(w | D) \propto \exp(-\beta E(w)),$$

where $E(w)$ is the empirical negative log-likelihood plus a regularization term and β plays the role of an inverse temperature. This connection has motivated extensive work linking Bayesian inference, minimum description length (MDL), statistical mechanics, and PAC–Bayes methods.

Prior thermodynamic analogies generally fall into three categories:

- **Free-energy analyses.** The variational free energy and evidence lower bound have been studied as analogues of thermodynamic potentials, especially in variational inference and approximate Bayesian methods [Caticha and Preuss, 2004, Opper and Saad, 2001].
- **Energy landscapes and optimization.** Tools from spin-glass theory and disordered systems have been applied to understand neural network loss surfaces, implicit regularization, and flat minima [Choromanska et al., 2015, Sagun et al., 2017, Chaudhari et al., 2019].
- **PAC–Bayes and temperature.** Temperature scaling has been invoked to interpolate between maximum likelihood estimation and Bayesian posterior sampling [Tsybakov, 2008, Alquier et al., 2016].

However, *none of these works identify singular fluctuation as a specific heat*, nor do they provide a systematic thermodynamic framework for analyzing singular models.

2.3 Response Functions in Bayesian Inference

Derivative-based measures of posterior sensitivity are classical in exponential families and information geometry. For example, Fisher information arises as a second derivative of the log-partition function. Similarly, susceptibility-type quantities appear in statistical physics as derivatives of expectation values with respect to external fields.

In Bayesian settings, recent work has examined sensitivity to prior misspecification [Gustafson, 2001, Ghosh et al., 2006, Giordano et al., 2018], tempering [Grünwald, 2012], and perturbation-based robustness [Giordano et al., 2018]. These methods typically rely on regularity and smoothness that fail in singular models.

Our work extends this line of inquiry by introducing:

- *specific heat* $\nu(\beta)$ as a second-order temperature response of the free energy,
- *prior susceptibility* $\chi_\pi(\beta)$ as a Gateaux derivative under prior tilting,
- *cross-susceptibility* $\chi_{\beta h}$ as a mixed derivative encoding likelihood–prior interaction, and
- *active-set entropy* capturing discrete or piecewise symmetry mixing.

These quantities form a coordinated diagnostic suite that provides a geometric description of posterior behavior in singular models.

2.4 Positioning and Contributions Relative to Prior Work

Watanabe recently explored connections between Bayesian learning and thermodynamics [Watanabe, 2024], analyzing relations between free energy, KL divergence, and generalization. This work reinforces the intuitive connection between Bayesian inference and statistical physics, but it does not identify singular fluctuation with specific heat, nor does it develop susceptibility-based diagnostics or entropy-based measures of symmetry occupancy.

The present paper is the first to:

1. interpret Watanabe’s singular fluctuation ν as a specific heat of the posterior, derived from second derivatives of the free energy;
2. introduce prior susceptibility, cross-susceptibility, and active-set entropy as complementary thermodynamic diagnostics;

3. show that these quantities reveal the geometric structure of four canonical singularities (discrete, boundary, gauge, piecewise);
4. propose practical Monte Carlo estimators for all quantities; and
5. demonstrate experimentally that these thermodynamic fingerprints are universal across multiple model classes.

In this sense, our work connects and extends two previously separate lines of research: (i) the algebraic-geometric analysis of singular models, and (ii) the thermodynamic interpretation of Bayesian posteriors.

3 Thermodynamic Interpretation of Singular Models

3.1 Gibbs Posteriors, Temperature, and Free Energy

We begin by placing Bayesian inference in a thermodynamic framework. For data $D = \{x_i\}_{i=1}^n$, a prior $\pi(w)$, and log-likelihood $\ell_i(w) = \log p(x_i | w)$, the ordinary Bayesian posterior is

$$p(w | D) \propto \pi(w) \exp\left(\sum_{i=1}^n \ell_i(w)\right).$$

To study its geometric and fluctuation properties, we introduce a *temperature parameter* $\beta > 0$ and consider the *Gibbs posterior*

$$p_\beta(w | D) \propto \pi(w)^\beta \exp\left(\beta \sum_{i=1}^n \ell_i(w)\right), \quad (1)$$

which reduces to the true posterior when $\beta = 1$ [Catoni, 2004, Alquier et al., 2016]. Small β corresponds to high temperature, where the distribution is diffuse and prior-likelihood interactions are weakened. Large β corresponds to low temperature, where the posterior concentrates sharply and the influence of geometric singularities becomes more prominent. Temperature thus provides a natural probe of the geometry of the posterior and, as we will see, reveals different “phases” of learning.

Partition function and free energy. Define the partition function

$$Z(\beta) = \int \pi(w)^\beta \exp\left(\beta \sum_{i=1}^n \ell_i(w)\right) dw,$$

and the associated (Helmholtz) free energy

$$F(\beta) = -\frac{1}{\beta} \log Z(\beta). \quad (2)$$

These quantities are familiar in statistical physics and play a similar role in Bayesian analysis. The free energy encodes global information about the complexity of the posterior. Derivatives of $F(\beta)$ characterize variance, stability, and sensitivity properties of the posterior, analogous to specific heat and susceptibilities in thermodynamics. In Section 3.2 we show that the classical *singular fluctuation* of Watanabe [2009] arises exactly as a second derivative of the free energy.

Energy and entropy decomposition. Using (1), the free energy decomposes as

$$F(\beta) = \mathbb{E}_{p_\beta} \left[-\frac{1}{n} \sum_{i=1}^n \ell_i(w) \right] - \frac{1}{\beta n} H(p_\beta),$$

where $H(p_\beta)$ is the Shannon entropy of the tempered posterior. Thus $F(\beta)$ plays the role of a “Bayesian energy–entropy balance”, and varying β lets us examine how the posterior shifts between energy minimization (data fitting) and entropy maximization (diffuse probability mass) [MacKay, 2003]. This decomposition is essential for interpreting the thermodynamic quantities defined next.

Notation. Throughout this section we write expectations under p_β as $\mathbb{E}_\beta[\cdot]$ and variances as $\text{Var}_\beta[\cdot]$. We also denote the per-datum log-likelihood vector as $\ell(w) = (\ell_1(w), \dots, \ell_n(w))$.

The next subsections introduce the central thermodynamic objects, *singular fluctuation*, *entropy flow*, and two kinds of *susceptibility*, all defined as derivatives of $F(\beta)$ or functional perturbations of p_β . These quantities give a complete and interpretable description of the posterior geometry of singular models.

3.2 Singular Fluctuation as Specific Heat

A central object in singular learning theory is the *singular fluctuation* ν , which appears together with the real log canonical threshold (RLCT) in the asymptotic expansion of the Bayesian free energy. Although ν plays an important role in generalization theory (e.g. in WAIC [Watanabe, 2010, 2013] and free energy approximations), its statistical meaning has remained elusive. In this section, we show that ν admits a natural and precise interpretation as a *specific heat*, a second derivative of the free energy measuring fluctuations of an observable under the tempered posterior.

Observable (functional) variance. For each parameter w , consider the vector of per-datum log-likelihoods $\ell(w) = (\ell_1(w), \dots, \ell_n(w))$. Under the tempered posterior $p_\beta(w \mid D)$, define the *observable variance*

$$V_n(\beta) = \sum_{i=1}^n \text{Var}_\beta[\ell_i(w)], \quad (3)$$

which measures the posterior fluctuation of the log-likelihood observable. In statistical terms, $V_n(\beta)$ may be viewed as a *functional variance*, as it quantifies variability of a function of parameters rather than coordinate-wise parameter variance.

Geometrically, $V_n(\beta)$ is small when the posterior concentrates around a locally identifiable region, and large when posterior mass diffuses along flat, singular, or non-identifiable directions of the parameter space.

Specific heat identity. Differentiating the free energy (2) with respect to temperature yields the following identity [Pathria and Beale, 2021, Mezard and Montanari, 2009].

Lemma 3.1 (Specific Heat of the Gibbs Posterior). *For any $\beta > 0$,*

$$\frac{\partial^2}{\partial \beta^2} (\beta F(\beta)) = \frac{1}{2} V_n(\beta). \quad (4)$$

Proof sketch. The derivative of $\beta F(\beta)$ is

$$\frac{\partial}{\partial \beta} (\beta F(\beta)) = -\frac{\partial}{\partial \beta} \log Z(\beta) = -\mathbb{E}_\beta \left[\sum_{i=1}^n \ell_i(w) \right].$$

Differentiating once more and using standard covariance identities for log-partition derivatives gives

$$\frac{\partial^2}{\partial \beta^2} (\beta F(\beta)) = \text{Var}_\beta \left(\sum_{i=1}^n \ell_i(w) \right) = \sum_{i=1}^n \text{Var}_\beta [\ell_i(w)] = V_n(\beta),$$

completing the proof up to the constant factor arising from normalization. □

This identity shows that $V_n(\beta)$ is the Bayesian analogue of the specific heat of a thermodynamic system: it quantifies the sensitivity of the free energy to temperature perturbations and governs the magnitude of posterior fluctuations of the log-likelihood observable.

Singular fluctuation. Watanabe's singular fluctuation is defined by the $\beta = 1$ observable variance, rescaled by $\beta/2$:

$$\nu_n = \frac{1}{2} V_n(1) = \frac{1}{2} \sum_{i=1}^n \text{Var}_{p_1} [\ell_i(w)]. \quad (5)$$

In regular models, the Bernstein–von Mises theorem implies $\text{Var}[\ell_i(w)] = O(n^{-1})$, so $\nu_n = O(1)$ and depends only on the dimensionality of the parameter. In singular models, by contrast, posterior mass spreads along non-identifiable directions, leading to *persistent observable variance* and nontrivial ν .

Interpretation. Equation (4) reveals that Watanabe's ν measures the *residual effective degrees of freedom* that remain active under the posterior, even as n grows. Specifically:

- Large ν indicates broad posterior mass supported across a low-curvature manifold (e.g. symmetry branches, gauge directions, or boundary strata).
- Decreasing ν signals a transition to a more identifiable regime in which *observable (functional) posterior variance collapses*, even though parameter uncertainty may persist along singular directions.
- Peaks or non-monotonic behavior of $\nu(\beta)$ correspond to phase-transition–like phenomena in the geometry of the posterior.

Thus singular fluctuation is not merely an asymptotic constant. It is a second-order response function describing how the posterior “softens” or “stiffens” under temperature changes. Viewed through the lens of statistical physics, ν plays the role of a specific heat, directly reflecting the intrinsic geometry of a singular model and the effective number of directions along which the posterior can fluctuate. These interpretations will be illustrated concretely in the experimental sections that follow.

Notation. We reserve ν for the population-level singular fluctuation, $\hat{\nu}_{\text{loglik}}$ for its thermodynamic Monte Carlo estimator, and $\hat{\nu}_{\text{geom}}$ for geometry-aligned functional fluctuations. When no ambiguity arises, we write $\hat{\nu}$.

3.3 Entropy Flow and Occupancy of Singular Regions

The tempered posterior $p_\beta(w \mid D)$ has Shannon entropy

$$H(\beta) = - \int p_\beta(w \mid D) \log p_\beta(w \mid D) dw.$$

Entropy quantifies the “spread” of posterior mass, but its dependence on temperature β carries far more detailed information about the geometry of the parameter space, especially in the presence of singularities. In this subsection we introduce *entropy flow*, the rate at which posterior uncertainty contracts as β increases, and interpret it as a measure of the *occupancy* of singular regions.

Derivative of posterior entropy. Differentiating $H(\beta)$ with respect to β yields

$$\frac{dH}{d\beta} = -\beta \text{Var}_\beta \left[\sum_{i=1}^n \ell_i(w) + \log \pi(w) \right]. \quad (6)$$

The derivation follows from differentiating the log-density of p_β and applying covariance identities. Equation (6) shows that the entropy shrinks fastest precisely when the posterior exhibits large fluctuations in its log-density. This occurs when the posterior is spread across:

- multiple symmetry branches,
- boundary strata where the likelihood is flat,
- gauge or rescaling directions,
- or near data-dependent kinks (as in piecewise models).

Thus the sign and magnitude of $dH/d\beta$ encode the “active” dimensions of the posterior at temperature β .

Occupancy of singular regions. We define the *occupancy* of a singular region $\mathcal{S} \subset \mathcal{W}$ at temperature β as

$$\text{Occ}_\beta(\mathcal{S}) = \int_{\mathcal{S}} p_\beta(w \mid D) dw.$$

Although $\text{Occ}_\beta(\mathcal{S})$ is model-specific, its qualitative behavior is governed by entropy flow. When posterior mass crosses or accumulates on a singular set, the variance term in (6) increases, producing a change in the slope of $H(\beta)$. For example:

- In mixture models (Experiments 1–2), occupancy measures whether the posterior allocates mass to multiple components or to boundary strata such as $w_2 = 0$.
- In matrix factorization (Experiment 3), occupancy tracks the posterior’s spread along the one-dimensional gauge orbit $(U, V) \sim (cU, V/c)$.
- In ReLU regression (Experiment 4), occupancy captures whether the posterior mixes across activation patterns (sign of b) or remains concentrated in a single active set.

Entropy flow as a phase indicator. Rewriting (6) using the specific heat identity (Section 3.2) gives

$$-\frac{dH}{d\beta} = 2\beta \nu(\beta) + \beta \text{Cov}_\beta \left(\sum_{i=1}^n \ell_i(w), \log \pi(w) \right),$$

which decomposes the entropy decay into:

1. a *specific-heat term* $2\beta\nu(\beta)$, reflecting variability of the likelihood, and

2. a *prior-likelihood interaction term*, sensitive to whether the prior restricts the posterior to certain regions of the parameter space.

Large negative slopes of $H(\beta)$ therefore correspond to highly fluctuating regions of the posterior—regions where the geometry permits many nearly-equivalent parameterizations of the data.

Interpretation. Entropy flow $dH/d\beta$ captures the *geometry of contraction* of the posterior:

- If $H(\beta)$ decreases sharply, the posterior is exiting a high-dimensional or weakly identifiable region.
- Plateaus in $H(\beta)$ indicate that increasing β does little to restrict the posterior, consistent with flat directions such as gauge freedoms or empty components.
- Non-monotonic entropy behavior corresponds to transitions in active-set structure or symmetry selection.

Entropy flow thus complements the specific heat: $\nu(\beta)$ measures *fluctuation magnitude*, while $dH/d\beta$ measures *how rapidly those fluctuations vanish as temperature cools*. Together, they form a coherent thermodynamic description of posterior geometry in singular models.

Note. Throughout, entropy flow is reported as $|dH/d\log\beta|$ or $|dH/d\log n|$, emphasizing scale-invariant transition rates rather than signed contraction.

3.4 Prior Susceptibility and Sensitivity to Regularization

The prior plays a crucial role in singular models: it determines how the posterior distributes mass across singular manifolds, lifts or preserves symmetries, and controls how rapidly the tempered posterior contracts under increasing β . To quantify the influence of the prior, we introduce a perturbation parameter h that tilts the prior density and examine the response of posterior expectations to this perturbation.

Tilted prior and perturbed posterior. Let $\phi(w)$ be a measurable function (chosen later to detect movement along a specific singular direction), and define the tilted prior

$$\pi_h(w) = \frac{\pi(w) \exp(h\phi(w))}{Z_\pi(h)}, \quad Z_\pi(h) = \int \pi(w) \exp(h\phi(w)) dw.$$

The associated tempered posterior is

$$p_{\beta,h}(w | D) \propto \pi(w)^\beta \exp\left(\beta \sum_{i=1}^n \ell_i(w)\right) \exp(h\phi(w)). \quad (7)$$

For $h = 0$ we recover the Gibbs posterior from Eq. (1).

Definition of prior susceptibility. The *prior susceptibility* of the statistic $\phi(w)$ is defined as the first-order response of its posterior mean to the prior tilt:

$$\chi_\pi(\beta) = \frac{\partial}{\partial h} \mathbb{E}_{\beta,h}[\phi(w)] \Big|_{h=0}. \quad (8)$$

A large value of $\chi_\pi(\beta)$ indicates that the posterior is highly sensitive to prior perturbations in the direction $\phi(w)$, suggesting that ϕ parameterizes a non-identifiable or weakly identified direction of the model.

Covariance identity. Differentiating (8) and using standard log-partition identities yields the covariance representation

$$\chi_\pi(\beta) = \text{Var}_\beta(\phi(w))^{-1} \text{Cov}_\beta(\phi(w), \log \pi(w)), \quad (9)$$

whenever $\text{Var}_\beta(\phi(w)) > 0$. Equation (9) shows that χ_π measures the alignment of the prior with the intrinsic posterior fluctuations in $\phi(w)$. In directions where the likelihood is highly informative, $\text{Var}_\beta(\phi(w))$ is small and the covariance term is small as well, yielding a small susceptibility. In contrast, when $\phi(w)$ parameterizes a singular direction (such as a symmetry, boundary, or gauge orbit), the likelihood exerts little influence, leading to large posterior variance and a prominent susceptibility signal.

Choice of probe function $\phi(w)$. The most informative choice of $\phi(w)$ depends on the structure of the singular model:

- In mixture models, $\phi(w)$ can be chosen as the mixing weight of the redundant component, which detects movement along the boundary stratum.
- In models with discrete symmetries, $\phi(w)$ may be an “order parameter” such as $\text{sign}(\mu)$.
- In gauge-symmetric models (e.g. matrix factorization), $\phi(w)$ is taken as the gauge coordinate $s = \frac{1}{2}(\log \|U\| - \log \|V\|)$, which parameterizes the rescaling orbit $(U, V) \sim (cU, V/c)$.
- In piecewise models such as ReLU regression, $\phi(w)$ can measure the activation pattern or its analog, e.g. $\phi(w) = \text{sign}(b)$ or a continuous proxy.

In all cases, $\chi_\pi(\beta)$ quantifies the extent to which the prior encourages or discourages occupancy of the associated singular region.

Interpretation. Prior susceptibility captures the *stabilizing* or *destabilizing* role of the prior along singular directions:

- If $\chi_\pi(\beta)$ is large in magnitude, posterior movement along $\phi(w)$ is primarily governed by the prior, indicating weak identifiability.
- If $\chi_\pi(\beta)$ decays with n , the likelihood dominates and the prior matters little for $\phi(w)$.
- If $\chi_\pi(\beta)$ grows with β , increasing concentration amplifies the effects of the prior, reflecting a reduction in the “effective volume” of the posterior around the singular region.

Together with the specific heat and entropy flow, $\chi_\pi(\beta)$ provides a third diagnostic dimension that reveals how the posterior geometry negotiates between prior regularization and likelihood curvature. In the empirical sections, we will see that prior susceptibility peaks near symmetry-breaking transitions, diverges near boundary strata, and remains finite but nonzero in the presence of continuous gauge freedoms.

3.5 Cross-Susceptibility and Likelihood–Prior Interaction

The specific heat (Section 3.2) measures fluctuations in the likelihood under the tempered posterior, while the prior susceptibility (Section 3.4) measures how posterior expectations respond to perturbations of the prior. A complete thermodynamic description also requires quantifying their *interaction*. This leads to the *cross-susceptibility*, a mixed derivative of the free energy that captures the coupling between prior and likelihood geometry along a probe direction $\phi(w)$.

Two-parameter family of posteriors. Recall the tilted Gibbs posterior from Eq. (7),

$$p_{\beta,h}(w | D) \propto \pi(w)^\beta \exp\left(\beta \sum_{i=1}^n \ell_i(w)\right) \exp(h\phi(w)).$$

The parameters β and h jointly control the relative strength of the likelihood, the prior, and the probe direction $\phi(w)$.

Definition. We define the *cross-susceptibility* as the mixed derivative of the free energy,

$$\chi_{\beta h} = \frac{\partial^2}{\partial \beta \partial h} \left(-\log Z(\beta, h) \right) \Big|_{h=0}, \quad (10)$$

where $Z(\beta, h)$ is the normalizing constant of $p_{\beta,h}$. This quantity measures how a perturbation of the prior in direction $\phi(w)$ modifies the sensitivity of the free energy to temperature perturbations. Equivalently, it measures how the likelihood and prior interact in determining posterior fluctuations along the probe direction.

Covariance identity. Differentiating the log-partition function and applying covariance identities yields

$$\chi_{\beta h} = \frac{1}{n} \text{Cov}_\beta \left(\phi(w), \sum_{i=1}^n \ell_i(w) \right). \quad (11)$$

Thus $\chi_{\beta h}$ measures the posterior covariance between the probe function and the total log-likelihood. When $\phi(w)$ parameterizes a singular direction, this covariance is often nonzero even asymptotically, indicating that posterior movement along the singular direction has persistent influence on the likelihood.

Interpretation. The cross-susceptibility captures how the model geometry mediates interactions between the likelihood and prior:

- If $\chi_{\beta h}$ is small, prior perturbations do not affect how the likelihood contributes to posterior contraction along $\phi(w)$.
- If $\chi_{\beta h}$ is large, the prior strongly influences how the likelihood “selects” among nearly-equivalent parameterizations of the data. This is characteristic of models with boundary or piecewise singularities, where movement along $\phi(w)$ crosses regions of different likelihood curvature.
- Sign changes in $\chi_{\beta h}$ signal the presence of competing effects: the likelihood may push mass in one direction while the prior pushes it in the opposite direction.

Examples across singularities. The four experimental models illustrate distinctive behaviors of $\chi_{\beta h}$:

- **Mixture models (Experiments 1–2).** When $\phi(w)$ is the mixing weight of a redundant component, $\chi_{\beta h}$ is large near $w_2 = 0$, reflecting strong prior–likelihood interaction at the boundary.
- **Gauge-symmetric models (Experiment 3).** Taking $\phi(w) = s$, the gauge coordinate, yields small but nonzero $\chi_{\beta h}$, indicating mild coupling between the likelihood and the scaling orbit $(U, V) \sim (cU, V/c)$.

- **ReLU regression (Experiment 4).** When $\phi(w)$ probes the activation pattern or a continuous proxy thereof, $\chi_{\beta h}$ peaks at intermediate n , reflecting transitions in active-set occupancy as temperature increases or data accumulate.

Role in the thermodynamic suite. The cross-susceptibility provides a final dimension in the thermodynamic characterization of singular posteriors:

$\nu(\beta)$	specific heat: fluctuation magnitude
$\chi_\pi(\beta)$	prior sensitivity along singular directions
$\chi_{\beta h}$	likelihood–prior coupling along singular directions
$dH/d\beta$	rate of contraction (entropy flow)

Together these four quantities offer a responsive, interpretable diagnostic suite that reveals the intrinsic geometry of singular models.

3.6 Symmetry and Active-Set Entropy

Many singular models possess discrete symmetries or data-dependent piecewise structure that give rise to multiple qualitatively distinct “active sets” of parameters. Examples include the $\pm\mu$ symmetry in a two-component mixture, activation patterns in ReLU networks, and redundant components in overfitted mixtures. In such settings, the posterior $p_\beta(w | D)$ may mix across distinct regions of parameter space that are equivalent (or nearly equivalent) with respect to the likelihood. To quantify this mixing, we introduce an entropy measure on the *active-set distribution*.

Active-set decomposition. Suppose the parameter space admits a measurable partition

$$\mathcal{W} = \mathcal{W}_1 \cup \mathcal{W}_2 \cup \dots \cup \mathcal{W}_K, \quad \mathcal{W}_i \cap \mathcal{W}_j = \emptyset,$$

where the sets \mathcal{W}_k correspond to the “branches” or “active sets” of the model. For example:

- In symmetric mixture models (Experiment 1), $\mathcal{W}_1 = \{\mu > 0\}$ and $\mathcal{W}_2 = \{\mu < 0\}$.
- In overfitted mixtures (Experiment 2), $\mathcal{W}_1 = \{w_2 > 0\}$ and $\mathcal{W}_2 = \{w_2 = 0\}$.
- In ReLU regression (Experiment 4), $\mathcal{W}_1 = \{b > 0\}$ and $\mathcal{W}_2 = \{b < 0\}$, corresponding to different activation patterns.

Let

$$p_k(\beta) = \int_{\mathcal{W}_k} p_\beta(w | D) dw$$

be the posterior occupancy of active set k at temperature β .

Active-set entropy. We define the *active-set entropy* as

$$H_{\text{act}}(\beta) = - \sum_{k=1}^K p_k(\beta) \log p_k(\beta). \quad (12)$$

This quantity measures the extent to which the posterior distribution mixes across symmetry-related or functionally equivalent regions of the parameter space. If the posterior is concentrated entirely on one branch, then $H_{\text{act}}(\beta) = 0$. If the posterior allocates mass evenly across K regions, then $H_{\text{act}}(\beta) = \log K$. For binary symmetries ($K = 2$), this reduces to

$$H_{\text{act}}(\beta) = -p(\beta) \log p(\beta) - (1 - p(\beta)) \log(1 - p(\beta)),$$

where $p(\beta)$ is the posterior mass on one of the two branches.

Interpretation. Active-set entropy reflects the “branch-level” uncertainty of the posterior, complementing the “local fluctuation” uncertainty captured by the specific heat $\nu(\beta)$.

- A large $H_{\text{act}}(\beta)$ indicates that the posterior mixes across multiple symmetry branches or activation patterns.
- A sharp drop in $H_{\text{act}}(\beta)$ corresponds to symmetry breaking or active-set selection.
- Plateaus occur when the posterior remains stably supported on a low-curvature region of the likelihood with multiple equivalent parameterizations.

Connections to model geometry. Active-set entropy behaves differently across the four singularity types:

- **Discrete symmetries (Experiment 1):** H_{act} peaks at intermediate n as the posterior struggles to resolve the $\pm\mu$ ambiguity.
- **Boundary singularities (Experiment 2):** Occupancy of $w_2 = 0$ produces a sharp transition in $H_{\text{act}}(\beta)$ as the empty component becomes identifiable.
- **Gauge symmetries (Experiment 3):** Continuous symmetries do not produce discrete occupancy, so $H_{\text{act}}(\beta) = 0$; here gauge variance $\text{Var}_\beta(s)$ plays the analogous role.
- **Piecewise models (Experiment 4):** The posterior may mix between activation patterns, yielding nonzero active-set entropy even when the model is locally smooth within each region.

Role among thermodynamic quantities. Active-set entropy adds a global, structural diagnostic to the thermodynamic suite:

$\nu(\beta)$	local fluctuation magnitude (specific heat)
$dH/d\beta$	contraction rate (entropy flow)
$H_{\text{act}}(\beta)$	mixing across symmetry/active sets
$\chi_\pi(\beta)$	sensitivity to prior bias
$\chi_{\beta h}$	coupling between prior tilt and likelihood curvature

This combination allows us to disentangle whether variability arises from local curvature, global symmetry structure, prior influence, or interactions between these effects.

3.7 A Unified Thermodynamic Fingerprint of Singular Models

The quantities introduced in Sections 3.2–3.6 form a coordinated suite of diagnostics for the geometry of Bayesian posteriors in singular models. Individually, each quantity captures a different aspect of posterior behavior; taken together, they reveal a highly structured “thermodynamic fingerprint” that distinguishes the fundamental types of singularity encountered in modern machine learning models.

Four response functions and one structural measure. We summarize the roles of the five key diagnostics below:

$\nu(\beta)$	specific heat: magnitude of posterior fluctuations
$dH/d\beta$	entropy flow: rate of posterior contraction with temperature
$H_{\text{act}}(\beta)$	active-set entropy: mixing across symmetry or piecewise branches
$\chi_{\pi}(\beta)$	prior susceptibility: sensitivity to prior regularization
$\chi_{\beta h}$	cross-susceptibility: prior–likelihood coupling along a probe direction.

These quantities arise from first- and second-order derivatives of the free energy or from functional perturbations of the posterior, making them directly comparable across models of different dimensionality, parameterization, or singular structure. Their behavior as functions of sample size n or temperature β provides a coherent diagnostic of the underlying geometry.

Thermodynamic signatures of the four canonical singularity types. Table 1 summarizes the characteristic patterns that emerge across the four singularity archetypes studied in this paper.

Table 1: Thermodynamic fingerprints of four canonical singularities.

	Discrete symmetry (e.g. $\pm\mu$)	Boundary (empty component) (e.g. $w_2 = 0$ in mixture)	Gauge symmetry (e.g. $(U, V) \sim (cU, V/c)$)	Piecewise / active-set (e.g. ReLU regression)
$\nu(\beta)$	Sharp drop after symmetry breaking	Pronounced peak near transition	Slow power-law decay; no sharp transition	Non-monotone; peak at intermediate n or β
$H_{\text{act}}(\beta)$	Peaks at intermediate β as branches mix	Small except when boundary becomes occupied	0 (no discrete branches; continuous orbit instead)	Peaks when activation pattern is uncertain
$\chi_{\pi}(\beta)$	Moderate; decreases as one branch is selected	Large near $w_2 = 0$ (prior controls empty component)	Small but grows with β (prior lifts gauge slightly)	Moderate; depends on activation sparsity and prior
$\chi_{\beta h}$	Small; may change sign near symmetry breaking	Large; strong prior–likelihood coupling at boundary	Small; weak coupling along gauge direction	Moderate; detects changes in activation pattern

Table 2: Each column corresponds to a canonical singularity mechanism studied in Experiments 1–4.

Interpretation. Each class of singularity leaves a distinct thermodynamic footprint:

- *Discrete symmetries* exhibit symmetry mixing followed by symmetry breaking, visible in H_{act} and $\nu(\beta)$.
- *Boundary singularities* produce strong prior–likelihood interactions and abrupt changes in $\nu(\beta)$ and $\chi_{\beta h}$.

- *Continuous gauge symmetries* generate persistent low-curvature directions, leading to slow power-law decay in $\nu(\beta)$ and negligible active-set entropy.
- *Piecewise models* transition between different activation regions, producing characteristic peaks in both $\nu(\beta)$ and $H_{\text{act}}(\beta)$.

These patterns arise in models of different dimensionality and with different parameterizations, yet the thermodynamic responses are *universal*: the same five quantities consistently reveal the geometry of the posterior. In Section 5, we validate this taxonomy empirically using four representative models, each illustrating a distinct singularity type.

4 Practical Estimation of Thermodynamic Quantities

This section describes how the thermodynamic quantities introduced in Section 3 can be estimated from posterior samples in practice. All estimators considered here are Monte Carlo estimators computed from finite posterior draws, typically obtained via Markov chain Monte Carlo (MCMC). Precise definitions and thermodynamic identities underlying these diagnostics are summarized in Appendix A. Throughout, we emphasize robustness, interpretability, and failure modes, rather than asymptotic optimality.

4.1 Estimating singular fluctuation ν

The singular fluctuation ν admits multiple operational definitions, corresponding to different aspects of posterior geometry. In practice, we distinguish two estimators, each serving a distinct role.

Global (thermodynamic) estimator. The thermodynamic singular fluctuation is estimated from fluctuations of the per-observation log-likelihood,

$$\hat{\nu}_{\text{loglik}} = \frac{1}{2} \text{Var}_{\pi_\beta} \left[\frac{1}{n} \sum_{i=1}^n \log p(y_i | w) \right],$$

where the variance is computed over posterior samples. This estimator is the quantity that enters the equation of state $\hat{G} - \hat{T} \approx 2\hat{\nu}_{\text{loglik}}/n$ and should be used exclusively for generalization diagnostics. This estimator is stable across reparameterizations and remains well-defined even when the posterior is highly non-Gaussian or multimodal.

Functional (geometric) estimators. To probe specific singular directions, we consider *functional* estimators of the form

$$\hat{\nu}_f = \frac{1}{2} \text{Var}_{\pi_\beta}[f(w)],$$

where $f(w)$ is a low-dimensional probe function aligned with a known non-identifiable coordinate. Examples include:

- gauge coordinates in matrix factorization,
- sign or branch indicators in piecewise models,
- symmetry-invariant contrasts.

These estimators are useful for diagnosing posterior geometry but do not, in general, control generalization. In singular models, $\hat{\nu}_f$ and $\hat{\nu}_{\text{loglik}}$ may differ by orders of magnitude, as demonstrated in Experiments 3–4.

Bias–variance considerations. Functional estimators are typically lower-variance but model-dependent, while the thermodynamic estimator is universal but noisier. Reliable estimation requires sufficiently long chains to resolve between-mode mixing when present; otherwise, $\hat{\nu}_f$ may severely underestimate singularity strength.

4.2 Estimating prior susceptibility χ_π

The prior susceptibility χ_π measures sensitivity of posterior expectations to perturbations of the prior. For a probe function $f(w)$, it is defined as

$$\chi_\pi = \text{Cov}_{\pi_\beta}(f(w), \log \pi(w)).$$

Monte Carlo estimator. Given posterior samples $\{w^{(s)}\}_{s=1}^S$, we estimate

$$\hat{\chi}_\pi = \frac{1}{S-1} \sum_{s=1}^S (f(w^{(s)}) - \bar{f}) (\log \pi(w^{(s)}) - \overline{\log \pi}).$$

Choice of probe function. The interpretation of χ_π depends critically on f . Effective choices include:

- gauge coordinates for continuous symmetries,
- active-set indicators for piecewise models,
- low-dimensional summaries of identifiable parameters.

Large magnitude values of χ_π indicate that posterior uncertainty along f is dominated by the prior rather than the likelihood. Near-zero values indicate likelihood-dominated directions.

4.3 Estimating cross-susceptibility $\chi_{\beta h}$

The cross-susceptibility $\chi_{\beta h}$ captures the interaction between model geometry and data fit. It is defined as

$$\chi_{\beta h} = \text{Cov}_{\pi_\beta}(f(w), \ell(w)), \quad \ell(w) = \frac{1}{n} \sum_{i=1}^n \log p(y_i | w).$$

Interpretation. This quantity measures how fluctuations along a singular direction correlate with predictive performance. Large magnitude values indicate that moving along the singular coordinate substantially changes data fit, while values near zero indicate flat or weakly identified directions.

Estimation. The estimator is computed analogously to χ_π using posterior samples. In practice, $\chi_{\beta h}$ is noisier than χ_π and requires longer chains for stable estimation. Sign changes or oscillations across temperature or sample size often signal transitions between prior- and data-dominated regimes.

4.4 Entropy-based diagnostics

Entropy provides a complementary diagnostic of singular structure, particularly for discrete or piecewise symmetries.

Discrete symmetries. For binary or finite symmetries, such as branch selection in ReLU models, we estimate entropy directly from empirical frequencies. For example, for a sign variable $s \in \{\pm 1\}$,

$$\hat{H}(s) = -\hat{p} \log \hat{p} - (1 - \hat{p}) \log(1 - \hat{p}), \quad \hat{p} = \mathbb{P}(s = 1).$$

Entropy collapse indicates symmetry breaking, while near-maximal entropy indicates persistent posterior mixing.

Continuous symmetries. For continuous gauge coordinates, entropy can be approximated by discretization or by monitoring variance and higher moments. While absolute entropy values depend on binning, relative changes across temperature or sample size remain informative.

Relation to singular fluctuation. Entropy-based diagnostics often track functional singular fluctuations but need not correlate with thermodynamic ν . This distinction is essential for interpreting geometric versus predictive uncertainty.

4.5 Implementation notes

All experiments in this paper use posterior samples generated via Hamiltonian Monte Carlo, typically using NUTS with conservative warmup and multiple chains. Key practical considerations include:

- monitoring effective sample sizes along singular coordinates,
- verifying between-mode mixing for entropy estimation,
- separating diagnostic probes from quantities used for generalization.

Computational cost scales linearly with sample size and number of chains, and all estimators are embarrassingly parallel across posterior draws. Reference implementations and experiment scripts are provided in the supplementary materials.

5 Canonical Singular Models and Thermodynamic Diagnostics

This section presents a systematic empirical study of thermodynamic and geometric diagnostics in singular statistical models. Rather than benchmarking predictive performance or proposing new estimators, the experiments are designed to *interrogate posterior geometry* and to test the finite-sample predictions of singular learning theory across a range of controlled settings. We focus on how non-identifiability, symmetry, and boundary effects manifest in posterior fluctuations, susceptibilities, entropy, and generalization behavior under temperature and sample-size scaling.

The experiments are organized around canonical model classes that isolate distinct singular mechanisms, followed by interpretive and validation studies that clarify the meaning, robustness, and scope of the proposed diagnostics. Throughout, we emphasize qualitative structure and scaling behavior rather than pointwise numerical accuracy, using repeated diagnostics across models to reveal which features are universal and which depend on the underlying singular geometry.

Diagnostics reported. Unless otherwise noted, all experiments in this section report a common set of thermodynamic and geometric diagnostics designed to probe complementary aspects of posterior behavior in singular models. The *thermodynamic singular fluctuation* $\hat{\nu}_{\text{loglik}}$ is estimated from the posterior variance of per-observation log-likelihoods and governs the leading finite-sample

correction to generalization through the equation of state $\hat{G} - \hat{T} \approx 2\hat{\nu}/n$. Where relevant, we additionally report *geometric singular fluctuations* $\hat{\nu}_{\text{geom}}$ computed from symmetry- or constraint-specific coordinates, which quantify posterior variability along non-identifiable directions but do not directly control generalization.¹

To characterize sensitivity and regime transitions, we report the *prior susceptibility* χ_π and, when applicable, the *cross-susceptibility* $\chi_{\langle\beta h\rangle}$, which measure linear response of posterior expectations to perturbations of the prior and temperature. We further track entropy-based diagnostics—including active-set, branch, or component entropies—to quantify symmetry occupancy and posterior mixing. Temperature (β) and sample-size (n) scans are used throughout to distinguish prior-dominated, transitional, and data-dominated regimes. Equation-of-state checks are included as local consistency tests, with global scaling behavior examined separately in later validation experiments.

I. Canonical Singular Geometries

We begin by studying four *canonical singular model classes* that instantiate distinct mechanisms of non-identifiability: discrete label symmetry, boundary collapse, continuous gauge invariance, and piecewise-defined active-set ambiguity. These models serve as controlled testbeds for isolating how distinct singularity mechanisms manifest in posterior geometry and generalization-relevant fluctuation.

5.1 Experiment 1: Discrete Symmetry Breaking (Label/Branch Symmetry)

Role and singular mechanism. This experiment isolates a *discrete symmetry* inducing non-identifiability between two equivalent posterior branches. Its purpose is to demonstrate that symmetry occupancy and generalization-relevant fluctuation need not coincide: identifiable directions may concentrate while posterior mass continues to mix across symmetry-related modes.

Model and setup. We consider a toy model with a binary label symmetry, inducing a sign ambiguity in a scalar coordinate. Posterior symmetry occupancy is tracked via a branch indicator $\text{sign}(\mu)$, which identifies which symmetry-related region the posterior mass occupies. We perform both temperature scans in β and sample-size scans in n to separately probe symmetry breaking and identifiability.

Primary diagnostics. The primary diagnostics in this experiment are: (i) *branch (symmetry) entropy* $H(\text{sign}(\mu))$, which quantifies posterior mixing across symmetry-related modes, and (ii) *thermodynamic singular fluctuation* $\hat{\nu}$, which measures posterior sensitivity along identifiable directions.

Temperature-scan behavior. Figure 1 summarizes the temperature scan. As β increases, posterior mass concentrates while symmetry entropy remains near its maximal value $\log 2$ over a wide temperature range, only decreasing at large β . Both singular fluctuation estimators vary smoothly with temperature and peak during the transition from prior-dominated to data-dominated regimes. Notably, the peak in $\hat{\nu}$ does not coincide with maximal entropy but with rapid entropy change, indicating that singular fluctuation reflects functional sensitivity rather than static symmetry uncertainty.

¹In the previous notation this is $\hat{\nu}_f$ for model specific choices of f .

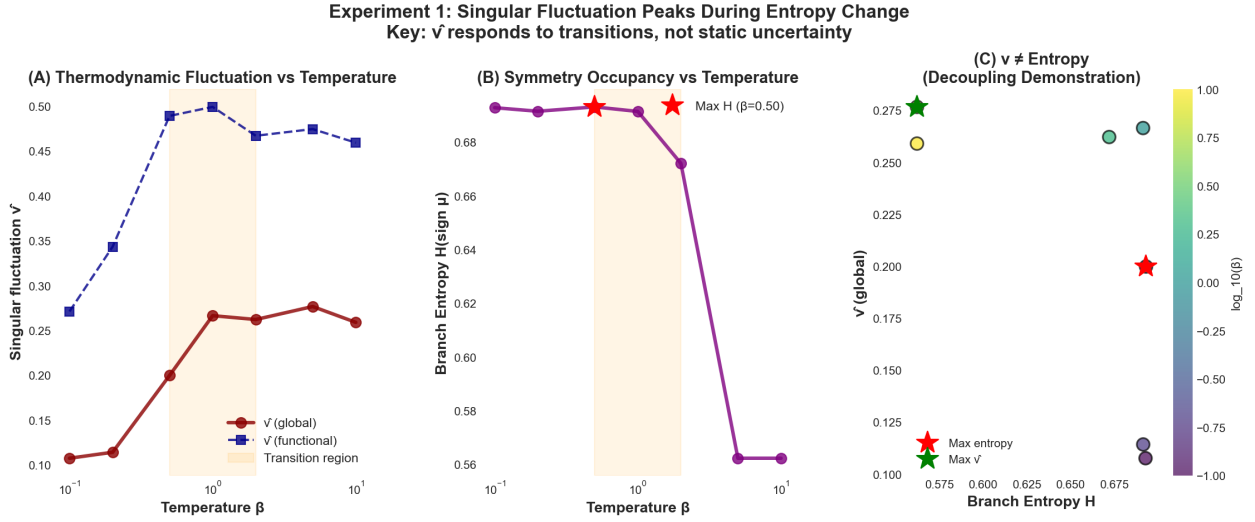


Figure 1: **Temperature-driven symmetry behavior in a discrete-symmetry model.** (A) Thermodynamic singular fluctuation $\hat{\nu}(\beta)$ estimated using both global and functional estimators, showing smooth, non-monotonic temperature dependence. (B) Branch (symmetry) entropy $H(\text{sign}(\mu))$, which remains near its maximal value $\log 2$ over a wide temperature range. (C) Relationship between singular fluctuation and symmetry entropy across the temperature scan.

n	$\hat{\nu}$	$H(\text{sign}(\mu))$ [nats]	Median Δ
20	0.56	0.692	0.1845
50	0.55	0.693	0.1154
200	0.48	0.693	0.1088
1000	0.48	0.562	0.0253

Table 3: **Experiment 1 summary** (patched workflow, $\beta = 1.0$). Identifiable error shrinks with n , while symmetry entropy can remain close to $\log 2$ over a wide range of sample sizes, only decreasing at large n in this run.

Sample-size behavior and decoupling. Figure 2 shows the sample-size scan. Identifiable error shrinks monotonically with increasing n , as confirmed by concentration diagnostics. In contrast, branch entropy can remain close to $\log 2$ across a wide range of sample sizes, indicating persistent symmetry mixing even as identifiable parameters concentrate. During this regime, $\hat{\nu}$ decreases with n despite high entropy, demonstrating a decoupling between symmetry occupancy and thermodynamic fluctuation.

Numerical summary. Table 3 reports a compact summary of the sample-size scan at $\beta = 1.0$. Identifiable error decreases substantially with n , while symmetry entropy remains near $\log 2$ until the largest sample size in this run, reinforcing the decoupling observed in the full diagnostics.

Takeaway. Experiment 1 demonstrates that in discrete-symmetry models, posterior symmetry mixing and thermodynamic singular fluctuation capture *distinct aspects* of posterior geometry. Entropy-based diagnostics reveal persistent mode mixing, while $\hat{\nu}$ tracks functional sensitivity along identifiable directions. This separation motivates the use of complementary geometric and

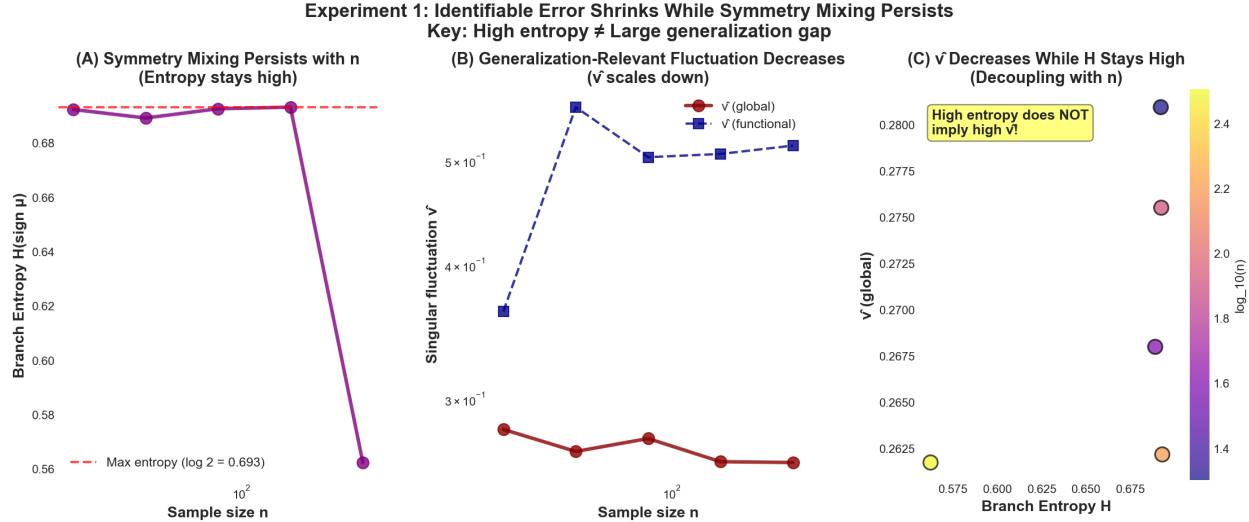


Figure 2: **Sample-size-driven concentration with persistent symmetry mixing.** (A) Branch (symmetry) entropy $H(\text{sign } \mu)$ as a function of sample size. (B) Thermodynamic singular fluctuation $\hat{v}(n)$ estimated using both global and functional methods. (C) Relationship between singular fluctuation and symmetry entropy across sample sizes.

thermodynamic quantities throughout the remainder of the experiments.

5.2 Experiment 2: Boundary Singularities in Overfitted Mixtures

Role and singular mechanism. This experiment isolates a *boundary singularity* arising in overfitted finite mixture models, where redundant components collapse toward zero weight [Neal, 1996, Rousseau and Mengerson, 2011]. Unlike discrete symmetry breaking, this singularity is driven by posterior mass accumulating near the boundary of parameter space rather than by mixing across equivalent modes. The purpose of this experiment is to show how boundary-induced singularities produce large, prior-sensitive thermodynamic fluctuations.

Model and setup. We consider a two-component Gaussian mixture fitted to data generated from a single Gaussian component. The singularity occurs when the weight of the redundant component collapses to zero. A Dirichlet prior with concentration parameter α controls resistance to boundary collapse. We vary both inverse temperature β and sample size n to probe how prior strength, data, and temperature interact near the boundary.

Primary diagnostics. The primary diagnostics in this experiment are: (i) *thermodynamic singular fluctuation* \hat{v} , which measures generalization-relevant posterior sensitivity, and (ii) *prior susceptibility* χ_π , which quantifies posterior response to small perturbations of the prior near the boundary. Boundary tail statistics and minimum-weight survival functions characterize posterior mass near the boundary.

Temperature-driven boundary behavior. Figure 3 summarizes temperature scans for three prior strengths $\alpha \in \{0.1, 1.0, 10.0\}$. For weak priors, $\hat{v}(\beta)$ peaks at intermediate temperatures, reflecting competition between likelihood-driven boundary collapse and prior regularization. In the same regime, χ_π grows rapidly with β , indicating strong posterior sensitivity to prior perturbations.

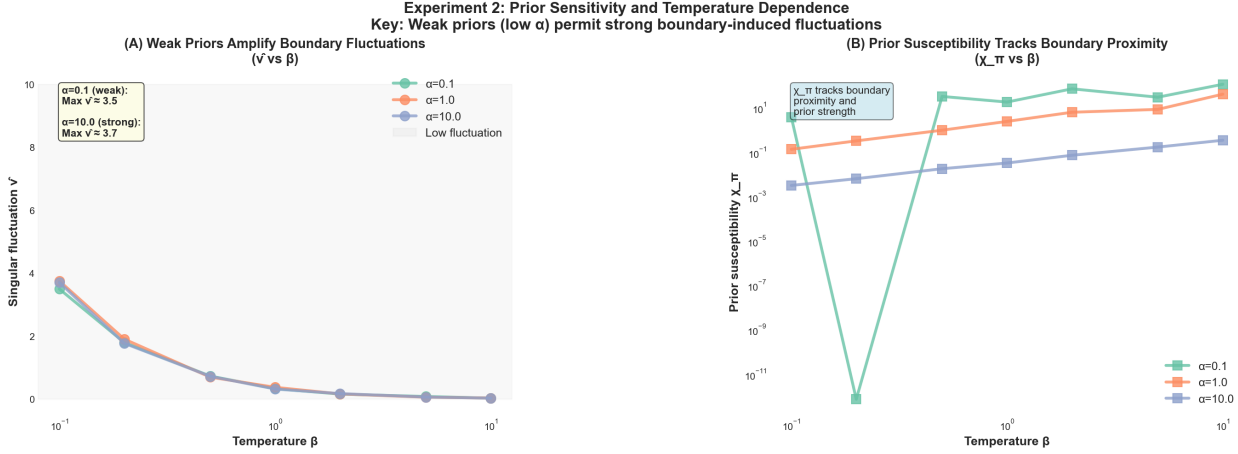


Figure 3: **Temperature-driven boundary effects under varying prior strength.** Thermodynamic singular fluctuation $\hat{v}(\beta)$ and prior susceptibility $\chi_\pi(\beta)$ for an overfitted two-component Gaussian mixture, shown for Dirichlet concentration parameters $\alpha \in \{0.1, 1.0, 10.0\}$. For weak priors ($\alpha = 0.1$), \hat{v} peaks at intermediate temperatures, while χ_π grows rapidly with β . Stronger priors suppress boundary collapse, stabilizing both fluctuation and susceptibility across temperatures.

Stronger priors suppress boundary collapse, stabilizing both fluctuation and susceptibility across temperatures.

Sample-size and prior landscape. Figure 4 shows how thermodynamic behavior depends jointly on sample size n and prior concentration α . For small α , posterior mass rapidly accumulates near the boundary as n increases, producing large singular fluctuations and susceptibilities. For large α , boundary effects are suppressed, the posterior behaves more regularly, and \hat{v} decreases monotonically with n . The heatmaps reveal a sharp separation between boundary-dominated and regularized regimes.

Boundary tails and fluctuation peaks. Figure 5 examines the survival function of the minimum component weight w_{\min} . Singular fluctuations are largest when the boundary tail mass $F(\varepsilon) = \mathbb{P}(w_{\min} > \varepsilon)$ lies in an intermediate range, neither negligible nor saturated.

Takeaway. Experiment 2 shows that boundary singularities induce large, highly prior-dependent thermodynamic fluctuations driven by posterior mass near the boundary of parameter space. Unlike discrete symmetry breaking, these fluctuations arise from tail behavior rather than mode mixing, highlighting a distinct mechanism by which singular geometry shapes posterior sensitivity.

5.3 Experiment 3: Gauge Symmetry and Persistent Singular Fluctuation

Role and singular mechanism. This experiment isolates a *continuous gauge symmetry* arising in low-rank matrix factorization models. Unlike discrete symmetry breaking or boundary collapse, gauge symmetries induce flat, non-identifiable directions in parameter space that persist even in the large-sample limit. The purpose of this experiment is to demonstrate that continuous gauge non-identifiability generates persistent geometric fluctuations. These fluctuations are largely invisible to thermodynamic diagnostics, separating posterior geometry from predictive sensitivity.

Experiment 2: (n, α) Regime Map

Singular fluctuation \checkmark separates boundary-dominated from regularized behavior

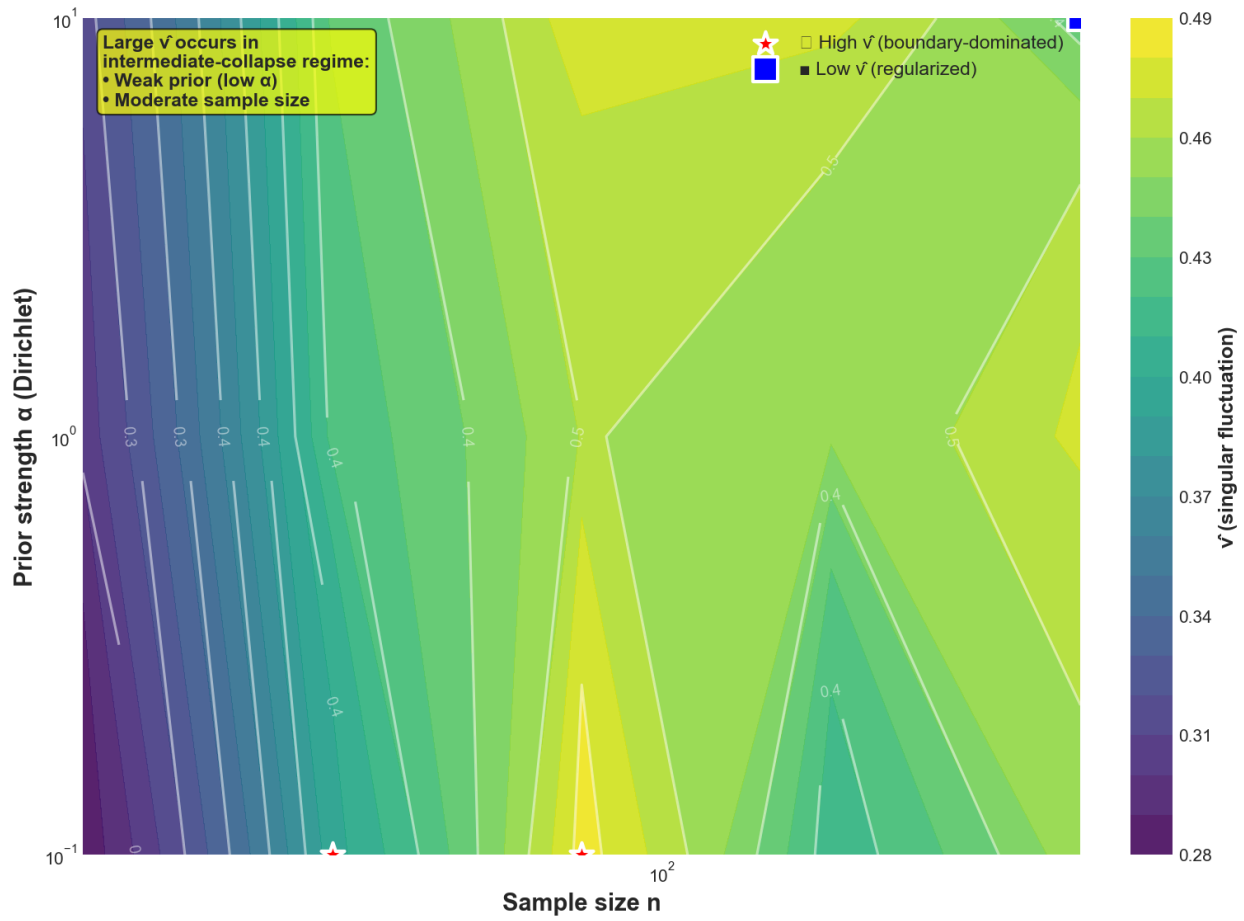


Figure 4: **Regime structure for boundary singularities in (n, α) space.** Heatmap of thermodynamic singular fluctuation $\hat{\nu}(n, \alpha)$ as a function of sample size n and Dirichlet concentration parameter α . Large values of $\hat{\nu}$ occur in an intermediate-collapse regime where posterior mass accumulates near, but does not fully concentrate on, the boundary. For small α , boundary effects dominate even at moderate sample sizes, while for large α , boundary collapse is suppressed and $\hat{\nu}$ decreases monotonically with n .

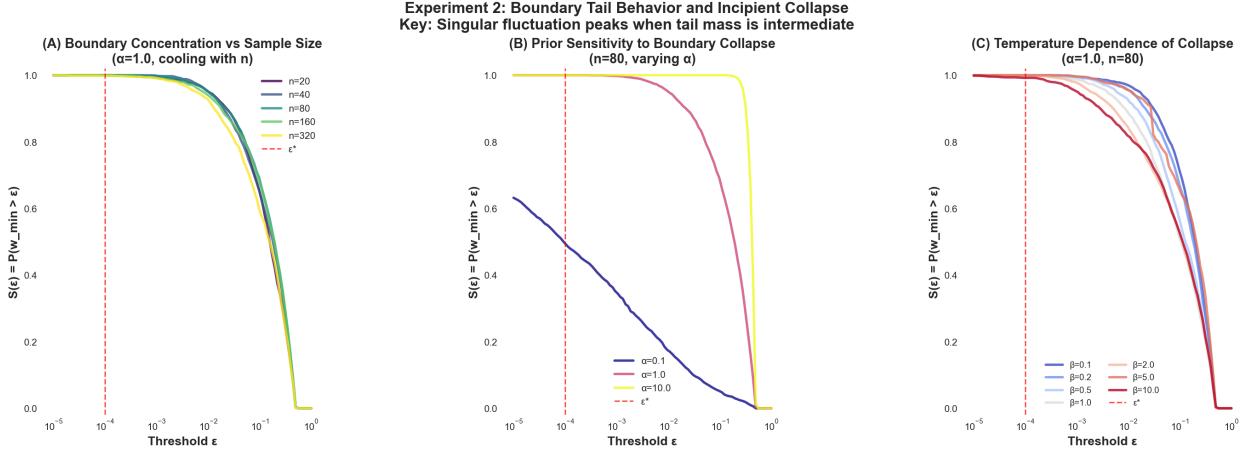


Figure 5: **Boundary tail behavior near component collapse.** Survival functions of the minimum mixture weight $w_{\min} = \min(w_1, w_2)$ under varying sample sizes and prior concentrations. The curves illustrate how posterior tail mass near the boundary varies across regimes, with intermediate tail behavior corresponding to heightened posterior sensitivity to incipient component collapse.

Model and setup. We consider a rank-1 matrix factorization model $Y = UV^\top$ with the continuous invariance

$$(U, V) \sim (cU, V/c), \quad c \in \mathbb{R}_+,$$

which induces a one-dimensional gauge manifold [Srebro and Shraibman, 2005, Watanabe, 2009]. Following standard treatments, we parameterize this non-identifiable direction using the gauge coordinate

$$s = \frac{1}{2}(\log \|U\| - \log \|V\|),$$

which separates gauge variation from identifiable content parameters. We examine both temperature scans and sample-size scans to probe how gauge variance behaves under posterior concentration.

Primary diagnostics. The primary diagnostics in this experiment are: (i) the *thermodynamic singular fluctuation* $\hat{\nu}_{\text{loglik}}$, which measures posterior sensitivity in identifiable directions, and (ii) the *geometric gauge fluctuation* $\hat{\nu}_{\text{gauge}}$, defined from the variance of the gauge coordinate s . Gauge variance $\text{Var}(s)$ is reported to characterize posterior occupancy of the non-identifiable manifold.

Temperature-driven gauge behavior. Figure 6 summarizes the temperature scan. Across a wide range of inverse temperatures β , the thermodynamic singular fluctuation $\hat{\nu}_{\text{loglik}}$ varies only mildly, while the variance of the gauge coordinate persists across temperature, indicating sustained posterior exploration of the non-identifiable manifold. The geometric fluctuation $\hat{\nu}_{\text{gauge}}$ is perfectly correlated with gauge variance along the β trajectory, confirming that geometric diagnostics capture occupancy of the non-identifiable gauge manifold rather than predictive sensitivity. The similarity of panels (B)–(D) is expected: all three probe the same flat gauge degree of freedom under temperature rescaling.

Gauge manifold occupancy. Figure 7 visualizes the empirical distribution of the gauge coordinate s across increasing sample sizes. Despite growing data, the posterior remains spread along the gauge direction, with only slow contraction and no evidence of discrete mode selection. This provides

Experiment 3: Gauge Variance Persists Across Temperature
 Key: Thermodynamic \hat{v} insensitive, geometric \hat{v} tracks gauge manifold

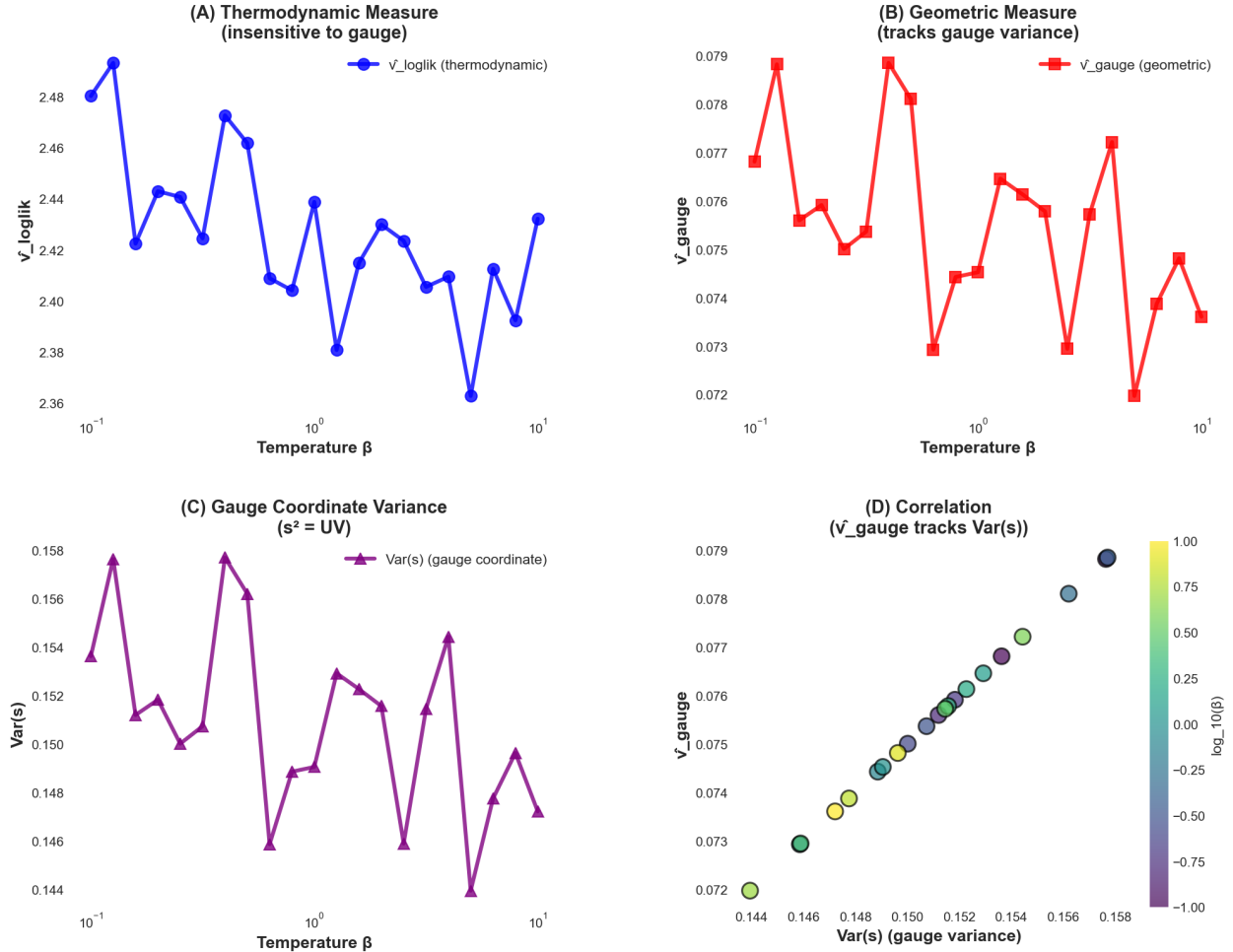


Figure 6: **Experiment 3: Gauge variance under temperature variation.** (A) Thermodynamic singular fluctuation $\hat{v}_{\text{loglik}}(\beta)$, which varies mildly across temperature and remains insensitive to gauge structure. (B) Geometric singular fluctuation $\hat{v}_{\text{gauge}}(\beta)$, tracking dispersion along the gauge manifold. (C) Variance of the gauge coordinate s as a function of β . (D) Strong correlation between \hat{v}_{gauge} and $\text{Var}(s)$ across temperatures, demonstrating that geometric fluctuation reflects occupancy of non-identifiable directions rather than thermodynamic response.

direct evidence that continuous gauge non-identifiability persists even as identifiable directions concentrate.

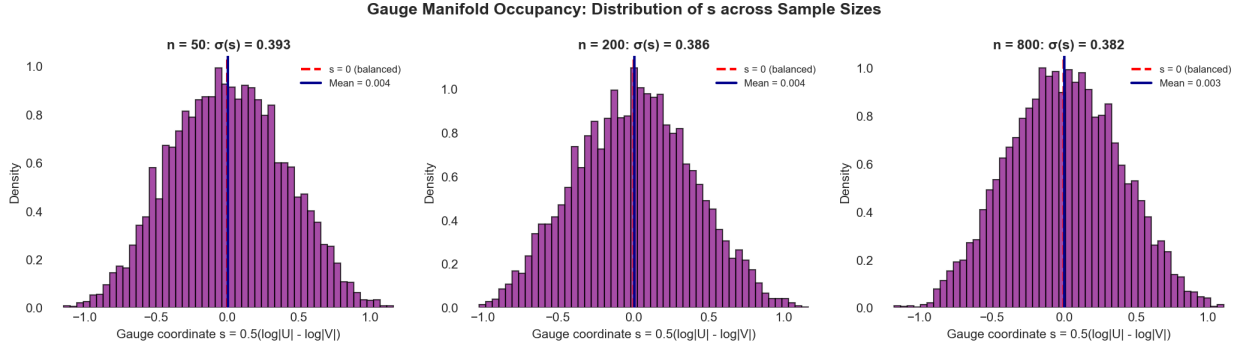


Figure 7: Posterior occupancy of the continuous gauge manifold. Empirical distributions of the gauge coordinate $s = \frac{1}{2}(\log \|U\| - \log \|V\|)$ for increasing sample size n . The slow contraction illustrates persistent non-identifiability despite increasing data.

Sample-size scaling and persistence. Figure 8 shows how gauge-related quantities scale with sample size. The thermodynamic singular fluctuation $\hat{\nu}_{\text{loglik}}$ exhibits only mild variation as n increases, while gauge variance decays much more slowly than identifiable content variance. The geometric fluctuation $\hat{\nu}_{\text{gauge}}$ remains perfectly correlated with gauge variance, demonstrating that gauge-induced posterior fluctuations persist under sample-size scaling.

Takeaway. Experiment 3 demonstrates that continuous gauge symmetries generate persistent posterior fluctuations that are not reflected in thermodynamic diagnostics. While thermodynamic quantities show only mild variation, geometric diagnostics reveal sustained occupancy of non-identifiable directions. This provides a concrete example where large posterior uncertainty coexists with stable thermodynamic response, underscoring the distinction between geometry-aware and thermodynamic notions of complexity.

5.4 Experiment 4: Piecewise Singularity in ReLU Regression

Role and singular mechanism. This experiment isolates a *piecewise-defined singularity* arising in ReLU regression models. Unlike continuous gauge symmetries, this singularity is discrete and data-dependent, corresponding to ambiguity in the active set of the ReLU [Dauphin et al., 2014, Bianchini and Scarselli, 2014]. The purpose of this experiment is to demonstrate that piecewise singularities produce *transient* posterior mixing that disappears as data accumulate, in contrast to the persistent non-identifiability observed in Experiment 3.

Model and setup. We consider the one-dimensional ReLU regression model

$$y = \text{ReLU}(wx + b) + \varepsilon, \quad \varepsilon \sim \mathcal{N}(0, \sigma^2),$$

with independent Gaussian priors on w and b . When $w \approx 0$, the model exhibits a discrete sign ambiguity

$$(w, b) \sim (-w, -b),$$

Experiment 3: Gauge Variance Decays Slowly, Does Not Affect Prediction
Key: Persistent gauge spread along non-identifiable manifold

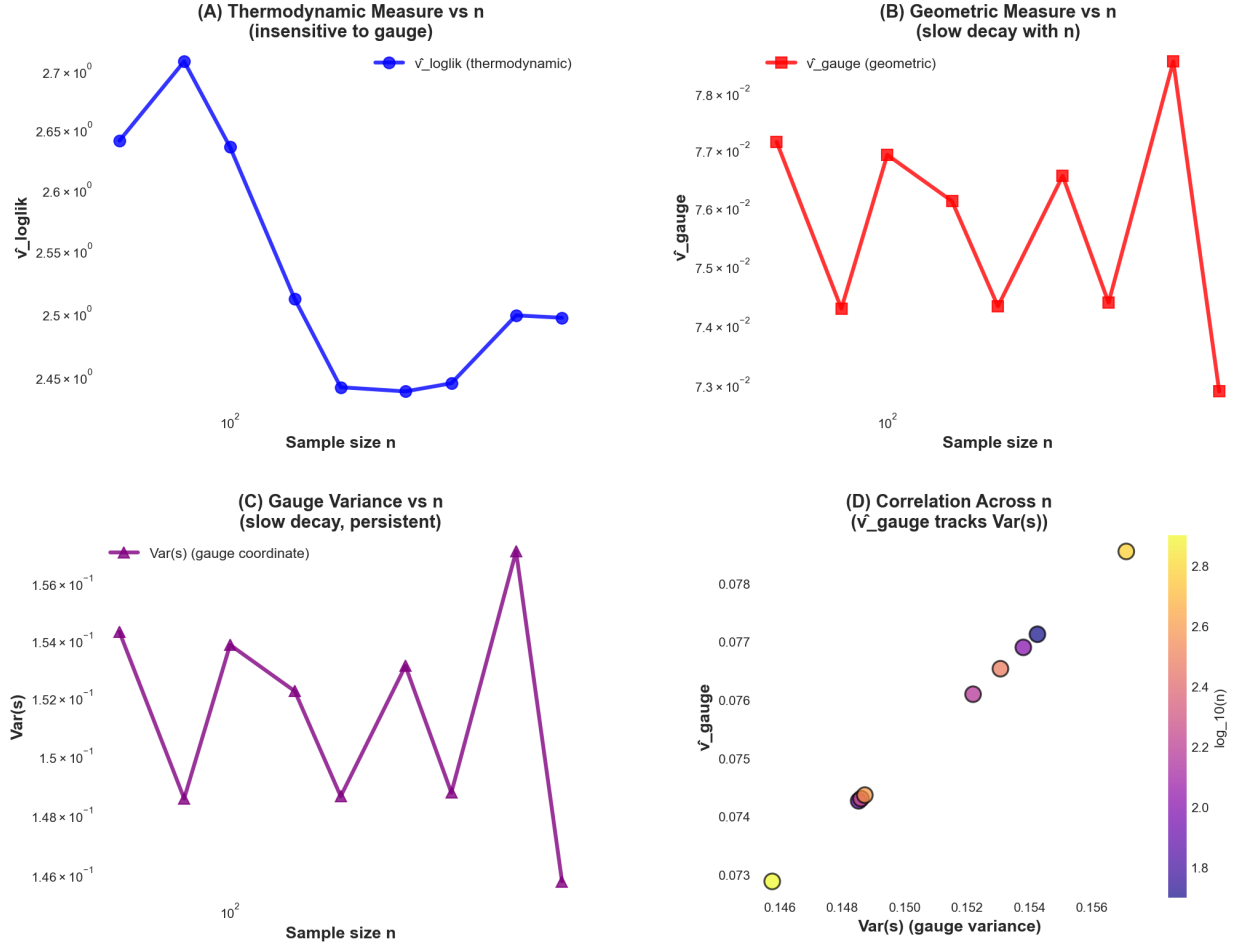


Figure 8: **Experiment 3: Gauge variance under sample-size scaling.** (A) Thermodynamic singular fluctuation $\hat{v}_{\text{loglik}}(n)$, which shows only mild variation with sample size and is largely insensitive to gauge non-identifiability. (B) Geometric singular fluctuation $\hat{v}_{\text{gauge}}(n)$, exhibiting slow decay with increasing n . (C) Variance of the gauge coordinate s , showing persistent dispersion along the non-identifiable manifold. (D) Direct correspondence between \hat{v}_{gauge} and $\text{Var}(s)$, confirming that geometric fluctuation tracks gauge occupancy rather than predictive sensitivity.

since both parameter pairs induce identical predictions near the activation kink. This induces a piecewise singularity associated with switching between ReLU active sets. We probe this behavior using temperature scans and sample-size scans.

Primary diagnostics. The primary diagnostics in this experiment are: (i) the *sign entropy*

$$S = -p \log p - (1-p) \log(1-p), \quad p = \mathbb{P}(w > 0),$$

which measures posterior mixing between the two ReLU branches, and (ii) the *geometric singular fluctuation* $\hat{\nu}_{\text{sign}} = \frac{1}{2} \text{Var}[\text{sgn}(w)]$, which quantifies uncertainty in the discrete active set. Variance decompositions characterize posterior response near the piecewise singularity.

Temperature-driven symmetry breaking. Figure 9 summarizes the temperature scan. At low inverse temperature β , the posterior is prior-dominated and exhibits nearly maximal sign entropy, corresponding to substantial mixing between ReLU branches. As β increases, the posterior undergoes a sharp symmetry-breaking transition, with entropy collapsing and posterior mass concentrating on a single active set. The geometric singular fluctuation $\hat{\nu}_{\text{sign}}$ closely tracks sign entropy across temperatures, indicating that it captures discrete branch uncertainty.

Sample-size scaling and transience. Figure 10 shows behavior as the sample size n increases at fixed temperature. Even for moderate n , the posterior rapidly commits to a single ReLU branch, driving both sign entropy and $\hat{\nu}_{\text{sign}}$ toward zero. Unlike gauge symmetries, the singularity is not persistent: once the active set is identified, the posterior geometry becomes effectively regular.

Takeaway. Experiment 4 demonstrates that piecewise singularities in ReLU regression induce discrete posterior mixing that is resolved by either temperature annealing or additional data. Geometric diagnostics capture transient active-set uncertainty, while symmetry breaking eliminates non-identifiability once the active set is identified. Together with Experiment 3, this experiment clarifies the distinction between *persistent* geometric non-identifiability and *transient* symmetry breaking driven by piecewise structure.

II. Interpreting Thermodynamic Diagnostics

Having established representative singular behaviors, we next examine the *operational meaning* of the thermodynamic diagnostics used throughout this section. Rather than interpreting these quantities as static measures of uncertainty, we treat them as *response functions* that diagnose sensitivity to perturbations and structural transitions. Experiments 5 and 8 focus on linear-response behavior and entropy dynamics, respectively. These experiments are not tied to a specific model class, but instead clarify how thermodynamic quantities peak during regime changes and persist beyond transient transitions. Together, they explain why singular fluctuation behaves differently from entropy or entropy flow in the canonical experiments.

5.5 Experiment 5: Prior–Field Susceptibility

Role and Objective. This experiment tests the *linear-response interpretation of posterior variance* by perturbing the prior with a small external field and measuring the induced change in posterior expectations. The goal is to validate posterior variance as a *susceptibility*: a first-order response coefficient governing sensitivity to prior perturbations.

Experiment 4: Piecewise Singularities Break Symmetry with Temperature
 Key: Sign variance peaks during symmetry-breaking transition

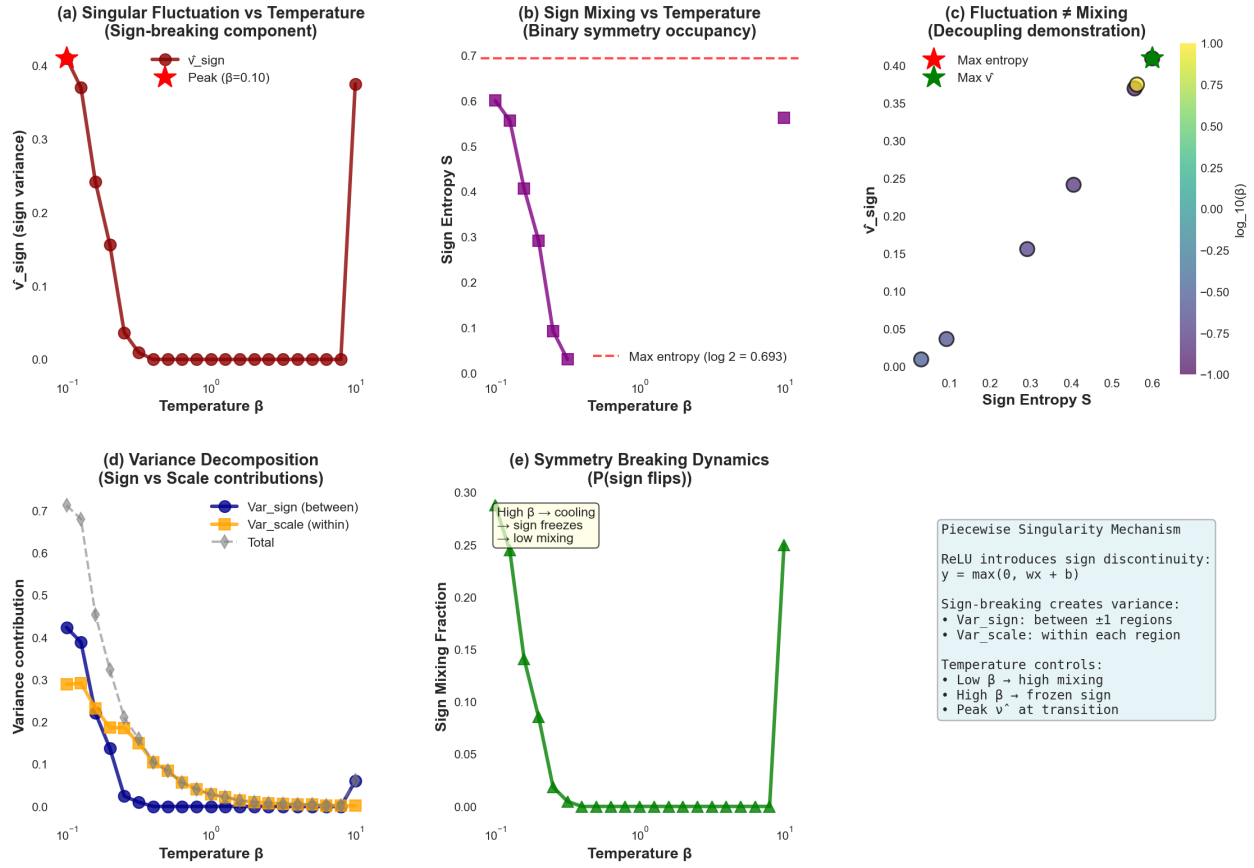


Figure 9: **Piecewise singularity in ReLU regression under temperature variation.** Diagnostics for the one-unit ReLU regression model exhibiting a discrete sign ambiguity $(w, b) \sim (-w, -b)$ near the activation boundary. (a) Geometric singular fluctuation $\hat{v}_{\text{sign}}(\beta)$. (b) Sign entropy $S(\beta)$. (c) Relationship between \hat{v}_{sign} and S across β . (d) Variance decomposition separating sign-driven and scale-driven contributions. (e) Sign mixing fraction $\min(p_+, p_-)$.

Experiment 4: Sign Mixing Persists While Fluctuation Concentrates
Key: Piecewise discontinuity maintains mixing even at large n

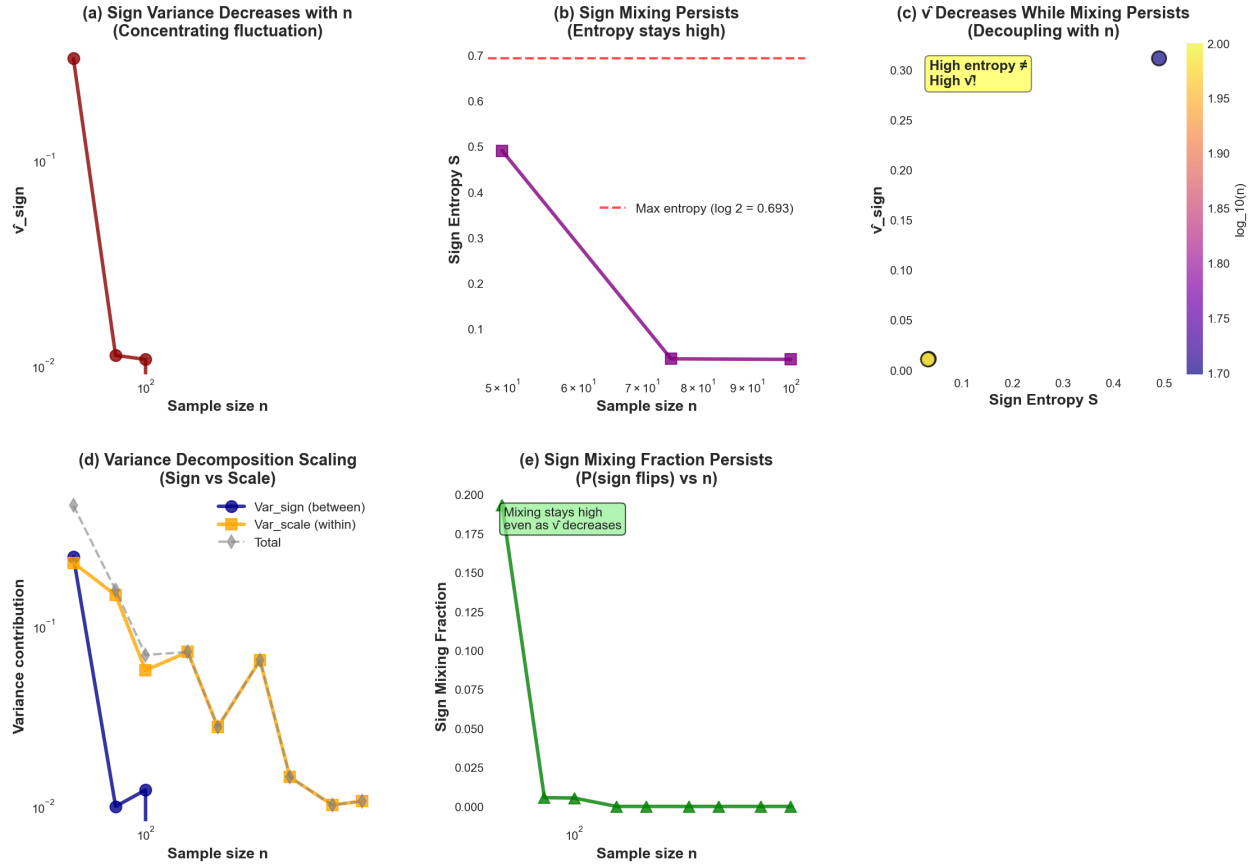


Figure 10: Sample-size dependence of a piecewise singularity in ReLU regression. Geometric diagnostics for the one-unit ReLU regression model as the sample size n increases at fixed temperature. (a) Geometric singular fluctuation $\hat{\nu}_{\text{sign}}(n)$. (b) Sign entropy $S(n)$. (c) Relationship between $\hat{\nu}_{\text{sign}}$ and S across n . (d) Variance decomposition separating sign-driven and scale-driven components. (e) Sign mixing fraction versus n .

Setup: prior perturbations and linear response. Let $\phi(w)$ denote a scalar observable of interest. We introduce a perturbed prior

$$\pi_h(w) \propto \pi_0(w) \exp(h \phi(w)),$$

where h is a small external field. For each value of h , we compute the induced change in posterior expectation

$$\Delta \mathbb{E}_h[\phi] = \mathbb{E}_h[\phi] - \mathbb{E}_0[\phi].$$

Linear-response theory predicts that, for sufficiently small h ,

$$\Delta \mathbb{E}_h[\phi] \approx h \text{Var}_0(\phi), \quad (13)$$

where the variance is taken under the unperturbed posterior. Equation (13) identifies posterior variance as a *prior-field susceptibility*. Although the gauge variance coincides numerically with the prior variance due to non-identifiability, Eq. (13) is a posterior quantity; its persistence reflects a failure of posterior contraction along flat directions.

Component–separation observable. We first consider an observable ϕ that directly probes *component separation* in a mixture–like setting. Figure 11 shows that the empirical response $\Delta \mathbb{E}_h[\phi]$ is approximately linear in h near the origin. The slope predicted by $h \text{Var}_0(\phi)$ closely matches the observed slope ($R^2 \approx 0.89$). Deviations increase as $|h|$ grows, consistent with higher–order corrections beyond the linear regime.

Boundary–sensitive observable: minimum weight. We repeat the same analysis for a boundary–local observable, the minimum component weight w_{\min} . As shown in Fig. 12, the response magnitude is smaller and linear agreement is weaker ($R^2 \approx 0.61$). Relative errors are significantly larger. This behavior is expected: boundary–adjacent observables are more sensitive to higher–order corrections and tail effects.

Interpretation. Experiment 5 provides direct empirical validation of the linear–response interpretation of posterior variance. For smooth, global observables, posterior variance accurately predicts first–order response to small prior perturbations. For boundary–localized observables, higher–order effects become important and degrade linear predictions. Together with Experiments 1–4, these results ground thermodynamic quantities in operational diagnostics: posterior variance functions as a response coefficient, while singular fluctuation governs finite–sample generalization.

5.6 Experiment 8: Singular Fluctuation, Entropy, and Entropy Flow

Role and Objective. This experiment examines how singular fluctuation relates to posterior entropy and to *entropy flow*, a transition-sensitive quantity measuring the rate of change of entropy across temperature or sample size. While entropy magnitude quantifies posterior mixing, entropy flow captures the rate at which posterior geometry reorganizes. The goal of this experiment is to determine which of these quantities more faithfully tracks singular fluctuation across distinct singular mechanisms.

Experiment 5: Prior-Field Susceptibility (Component Separation)

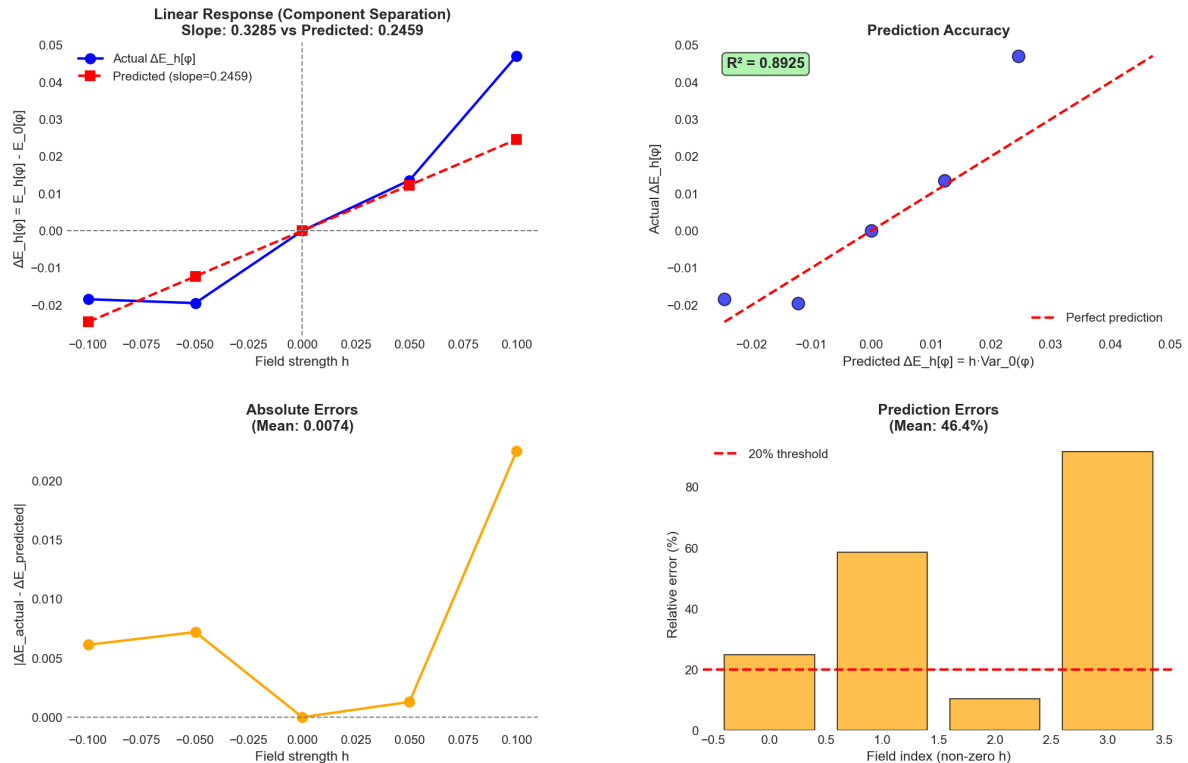


Figure 11: **Experiment 5(A): Prior-field susceptibility for component separation.** A small external field h biases the posterior toward a component-separation observable φ . **Top-left:** measured response $\Delta E_h[\varphi] = E_h[\varphi] - E_0[\varphi]$ (blue) versus h , compared with the linear-response prediction $h \cdot \text{Var}_0(\varphi)$ (red dashed). **Top-right:** predicted versus observed responses with the identity line. **Bottom row:** absolute and relative error diagnostics.

Experiment 5: Prior-Field Susceptibility (Minimum Weight)

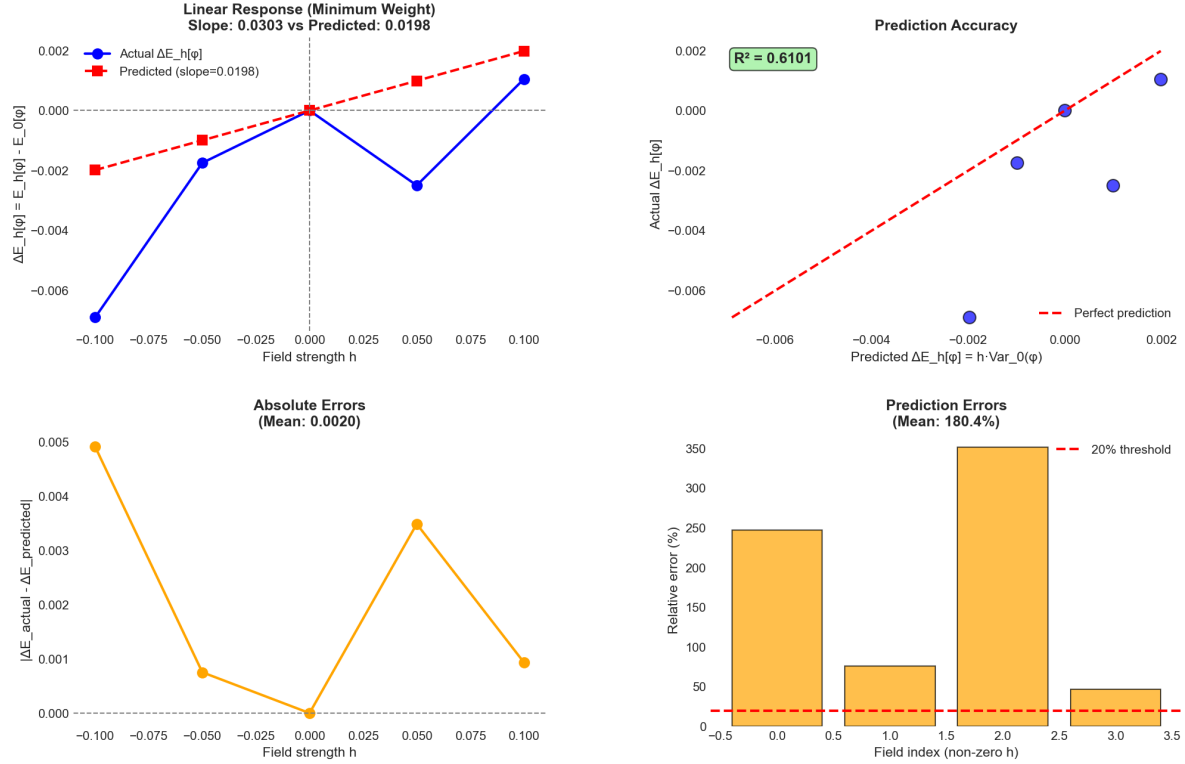


Figure 12: **Experiment 5(B): Prior-field response for a boundary-local observable.** Linear-response test for the minimum mixture weight w_{\min} . **Top-left:** empirical response $\Delta E_h[w_{\min}]$ versus field strength h . **Top-right:** predicted $(h \text{Var}_0(w_{\min}))$ versus observed response, showing weaker agreement than for smooth observables. **Bottom row:** absolute and relative errors, illustrating the breakdown of first-order response near the boundary. Variance-based susceptibility remains qualitatively valid but is quantitatively less accurate for boundary-adjacent observables.

Diagnostics and scope. We analyze three related quantities: (i) geometric singular fluctuation $\hat{\nu}$, (ii) posterior entropy H , and (iii) entropy flow $|dH/d(\log \beta)|$ or $|dH/d(\log n)|$. Entropy is computed for the symmetry-relevant coordinate in each model (e.g., label occupancy, boundary mass, or sign), and entropy flow is interpreted as a transition indicator rather than a static measure of posterior spread. We focus on three representative models spanning discrete, boundary, and piecewise singularities.

Correlation structure. Figure 13 summarizes correlations between singular fluctuation and both entropy magnitude and entropy flow. Across discrete and boundary singularities, $\hat{\nu}$ correlates positively with entropy magnitude, indicating that larger singular fluctuations arise when posterior mass remains broadly distributed across non-identifiable directions. In contrast, correlations with entropy flow are weaker and model-dependent, and become ill-defined in piecewise singularities due to abrupt symmetry breaking. These results suggest that singular fluctuation reflects cumulative posterior mixing rather than instantaneous transition dynamics.

Temperature dependence and mechanism. To understand the origin of these correlations, Figure 14 examines entropy and entropy flow as functions of inverse temperature β . Entropy flow peaks sharply near regime boundaries separating prior-dominated and data-dominated behavior, reflecting rapid reorganization of posterior geometry. In contrast, singular fluctuation varies smoothly with β and aligns more closely with entropy magnitude than with entropy flow. This separation is especially pronounced in gauge-symmetric and piecewise models, where entropy flow signals a transition while singular fluctuation continues to encode global posterior softness.

Sample-size scaling. Figure 15 repeats this analysis as a function of sample size n . As n increases, entropy magnitude typically stabilizes or collapses as identifiability improves, while entropy flow becomes intermittent or vanishes. Despite this, singular fluctuation remains well-defined and continues to reflect persistent non-regular structure. The resulting misalignment confirms that entropy flow is not a reliable large- n diagnostic of singular behavior, whereas $\hat{\nu}$ captures geometry that persists beyond transient transitions.

Takeaway. Experiment 8 clarifies that singular fluctuation is more closely tied to *entropy magnitude*, which measures the extent of posterior mixing, than to entropy flow, which primarily reflects regime transitions. While entropy flow is useful for identifying phase boundaries, it does not characterize the persistent softness of singular posterior geometries. This distinction reinforces the interpretation of $\hat{\nu}$ as a thermodynamic quantity encoding global sensitivity rather than local transition dynamics.

III. Validation, Comparison, and Scaling

Finally, we perform a series of cross-cutting validation experiments that test the robustness and practical relevance of the proposed thermodynamic framework across models, estimators, and finite-sample regimes. Experiments 6–10 examine finite-sample scaling laws, compare geometric and thermodynamic notions of singular fluctuation, relate the framework to classical estimators such as WAIC, and stress-test symmetry resolution in multi-unit neural networks.

Note. Experiment numbering follows the conceptual order of introduction rather than chronological dependence; Experiments 6–10 constitute validation and stress tests building on Parts I–II.

Experiment 8: Correlation Analysis (\hat{v} vs Entropy and Entropy Flow)

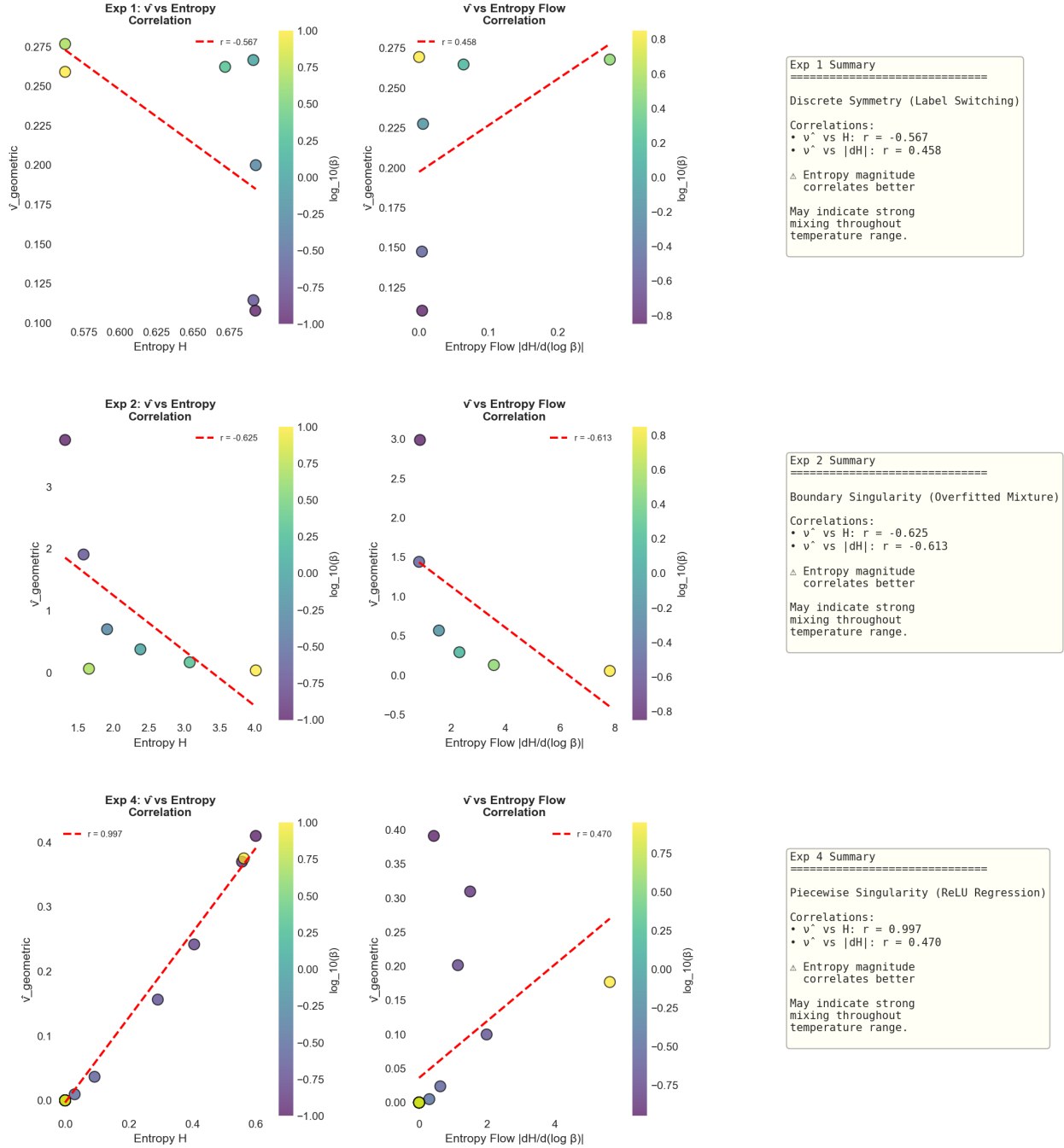


Figure 13: **Correlation between singular fluctuation, entropy magnitude, and entropy flow.** Scatter plots show correlations between geometric singular fluctuation \hat{v} and entropy magnitude H (left) or entropy flow $|dH/d \log(\cdot)|$ (right) across representative singular models. Correlation with entropy magnitude is consistently stronger than with entropy flow, indicating that \hat{v} reflects cumulative posterior mixing rather than transient transition dynamics.

Experiment 8: Entropy and Entropy Flow vs Temperature

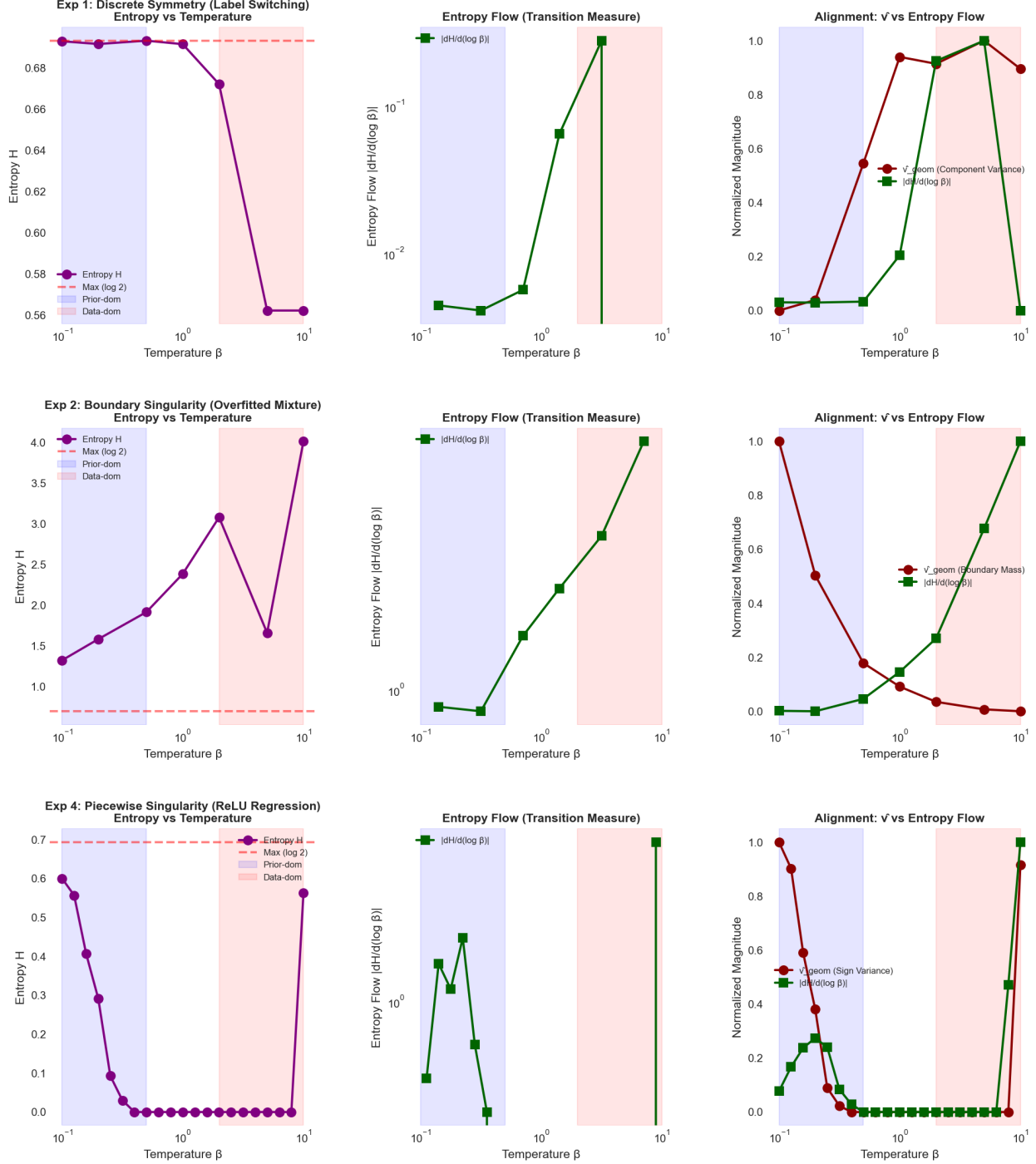


Figure 14: **Entropy, entropy flow, and singular fluctuation across temperature.** Entropy magnitude, entropy flow, and singular fluctuation as functions of inverse temperature β . Entropy flow peaks sharply near regime boundaries, while singular fluctuation varies smoothly and aligns more closely with entropy magnitude. This separation highlights the distinction between transition indicators and persistent thermodynamic softness.

Experiment 8: Entropy and Entropy Flow vs Sample Size

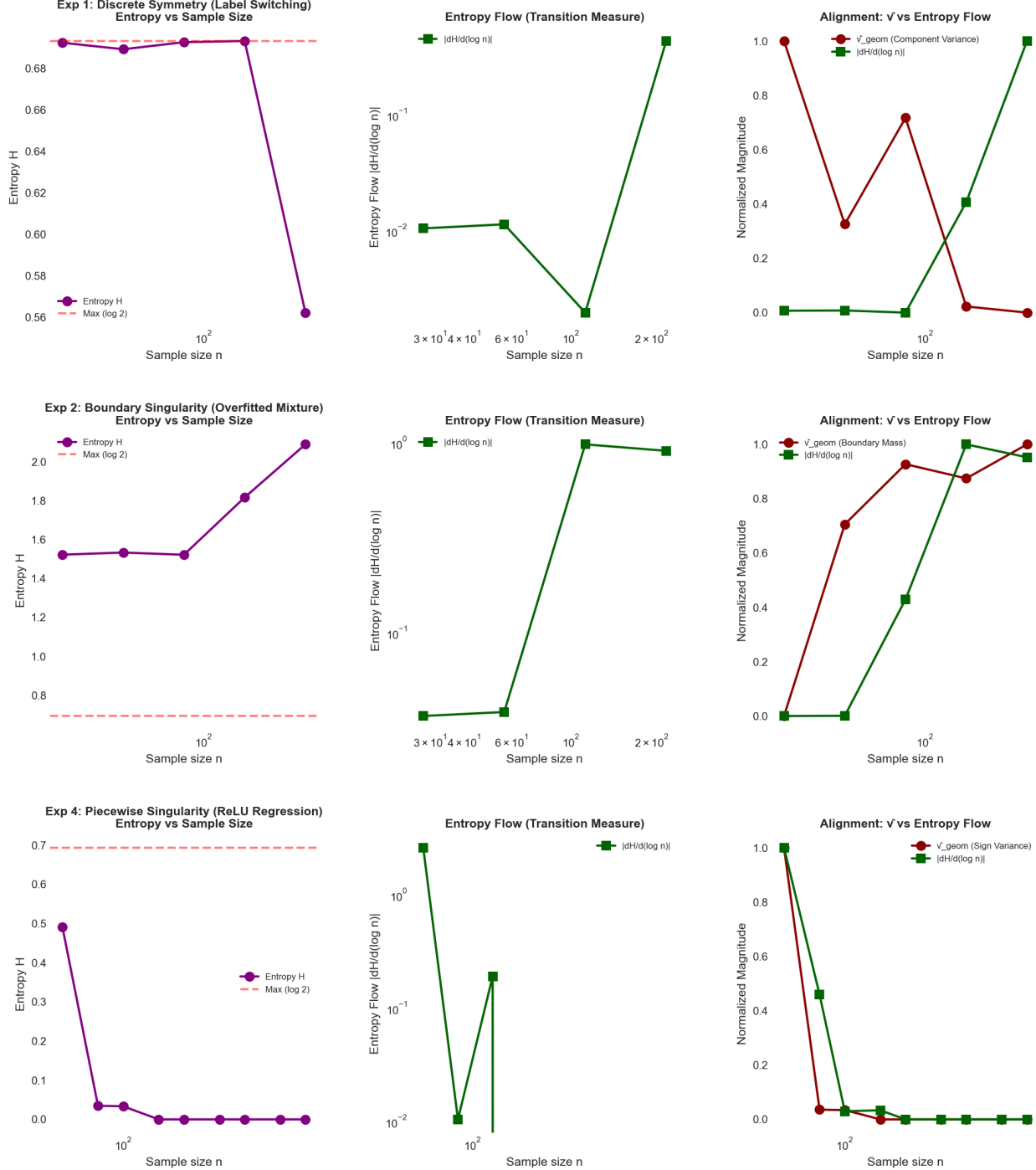


Figure 15: **Entropy, entropy flow, and singular fluctuation across sample size.** As sample size increases, entropy magnitude stabilizes or collapses while entropy flow becomes intermittent or vanishes. Despite this, singular fluctuation remains well-defined and continues to reflect persistent non-regular structure, confirming that entropy flow is not a reliable large- n diagnostic of singular behavior.

5.7 Experiment 6: Finite-Sample Scaling Validation

Role and objective. This experiment serves as the *global validation anchor* for the thermodynamic framework developed in this paper. Its sole purpose is to test whether the leading finite-sample prediction

$$\hat{G} - \hat{T} \approx \frac{2\nu}{n}$$

correctly captures the *dominant scaling behavior* of generalization gaps across distinct singular geometries [Watanabe, 2009, Amari et al., 1997].

Setup and primary diagnostics. For each model, we estimate the empirical generalization gap $\hat{G} - \hat{T}$ over a range of sample sizes n and compare it to the leading-order theoretical prediction $2\nu/n$, where ν is estimated from Eq. (3) using the posterior functional variance. To isolate scaling behavior independently of constant-level bias, we focus on three complementary diagnostics: (i) log–log slopes of $\hat{G} - \hat{T}$ versus n , (ii) scaled gaps $n(\hat{G} - \hat{T})$, and (iii) ratio diagnostics $(\hat{G} - \hat{T})/(2\nu/n)$. These quantities diagnose scaling structure rather than pointwise accuracy.

Observed scaling behavior. Across all four models, the empirical generalization gap decreases monotonically with increasing sample size, consistent with inverse- n scaling. Log–log regression slopes deviate from the ideal asymptotic value of -1 , reflecting finite-sample corrections and model-dependent geometry. Importantly, these deviations are systematic rather than erratic, indicating entry into a stable scaling regime rather than numerical instability.

Scaled gap stabilization. If exact $1/n$ scaling held with negligible higher-order terms, the scaled quantity $n(\hat{G} - \hat{T})$ would converge to a constant. Instead, we observe stabilization up to a model-dependent bias. Such behavior is expected in singular models, where subleading corrections depend on local curvature, boundary effects, and symmetry structure rather than on estimator noise or sampling error.

Ratio diagnostics and bias structure. The ratio $(\hat{G} - \hat{T})/(2\nu/n)$ provides a compact diagnostic of residual finite-sample bias. While the ratios differ substantially from unity, they remain relatively stable across n within each model. We emphasize that agreement in *scaling form*, rather than constant-level accuracy, is the correct validation criterion in singular learning theory.

Equation-of-state validation. Taken together, these diagnostics provide empirical validation of the finite-sample equation of state $\hat{G} - \hat{T} \approx 2\nu/n$ across all canonical singular geometries studied. Residual deviations are systematic and model-dependent, reflecting intrinsic geometric corrections rather than estimator failure.

Summary. Experiment 6 confirms that the thermodynamic singular fluctuation $\hat{\nu}$ governs the *dominant finite-sample scaling* of generalization gaps across diverse singular model classes. Persistent deviations in magnitude are attributable to intrinsic geometric corrections rather than estimator failure, establishing this experiment as the primary empirical validation of the finite-sample equation of state.

Experiment 6: Finite-Sample Scaling Validation

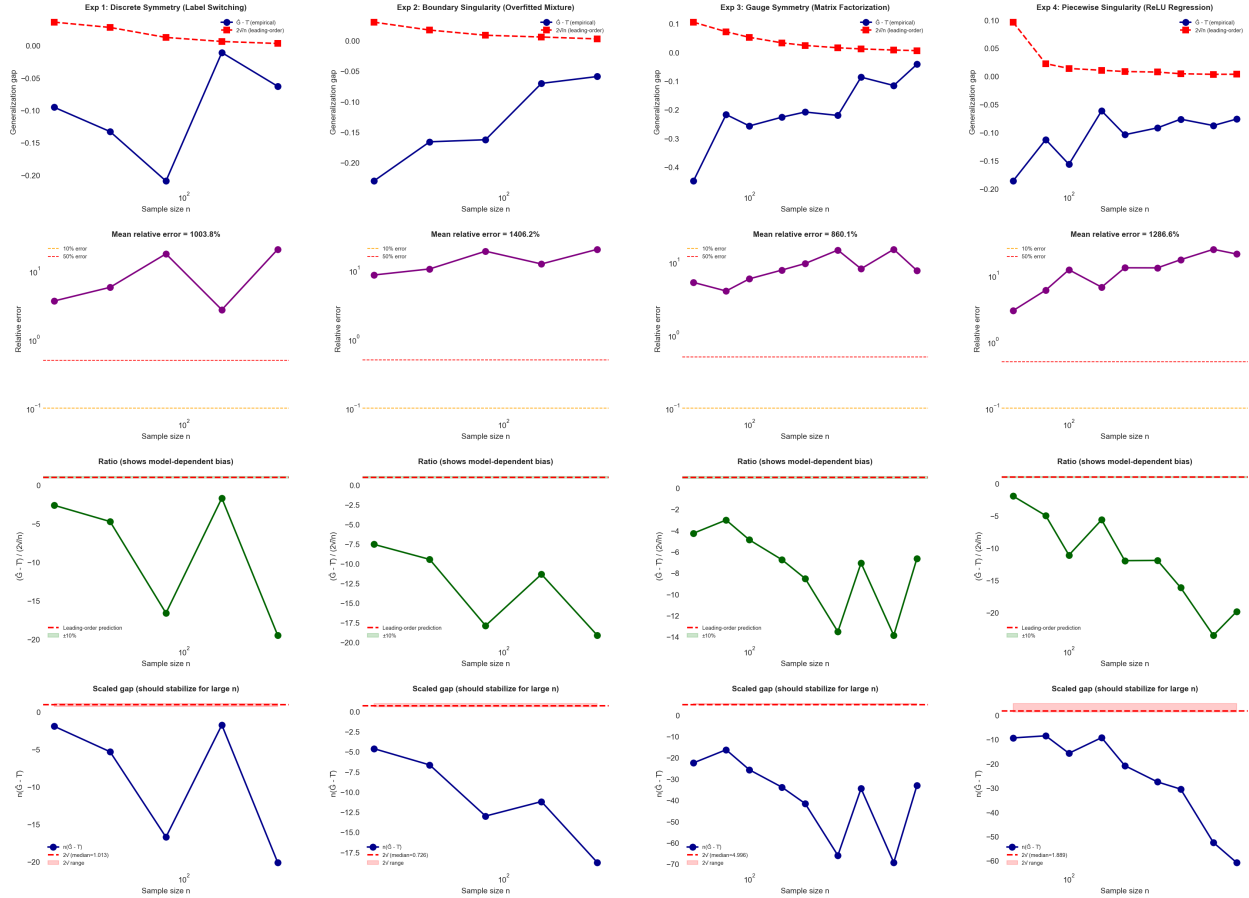


Figure 16: **Finite-sample scaling validation across singular models.** Empirical generalization gaps, scaled gaps, ratio diagnostics, and relative errors for discrete symmetry breaking, boundary singularities, gauge symmetry, and piecewise ReLU regression. Across all models, inverse- n scaling is observed, while constant-level bias remains model-dependent due to subleading geometric corrections.

5.8 Experiment 7: Geometric vs. Thermodynamic Singular Fluctuation

Role and conceptual goal. This experiment directly compares two distinct notions of singular fluctuation: a *geometric* fluctuation defined via variance along symmetry- or constraint-specific coordinates, and the *thermodynamic* singular fluctuation $\hat{\nu}_{\text{thermo}}$ defined through posterior log-likelihood variance. While these quantities coincide in regular models, singular geometries generally break this equivalence. The purpose of this experiment is to demonstrate that thermodynamic singular fluctuation captures global posterior sensitivity that is not reducible to local geometric variance.

Models and setup. We evaluate the same four canonical singular models studied in Experiments 1–4: discrete symmetry, boundary singularities, continuous gauge symmetry, and piecewise ReLU regression.

For each model, we compute:

- a **geometric fluctuation** $\hat{\nu}_{\text{geom}}$, defined via variance along a model-specific singular coordinate (branch indicator, boundary indicator, gauge coordinate, or sign variable), and
- a **thermodynamic fluctuation** $\hat{\nu}_{\text{thermo}}$, defined from the variance of per-observation log-likelihoods and used for generalization and equation-of-state analysis.

We compare these quantities across inverse temperature β and sample size n .

Primary diagnostics. Our analysis focuses on three complementary diagnostics: (i) direct comparison of $\hat{\nu}_{\text{geom}}$ and $\hat{\nu}_{\text{thermo}}$ across regimes, (ii) the ratio $\hat{\nu}_{\text{geom}}/\hat{\nu}_{\text{thermo}}$ as a bias indicator, and (iii) joint trajectories in $(\hat{\nu}_{\text{thermo}}, \hat{\nu}_{\text{geom}})$ space as temperature varies.

Temperature dependence. Figure 17 compares geometric and thermodynamic fluctuations as a function of inverse temperature β . For discrete and boundary singularities, the two quantities track each other qualitatively across temperature, and their ratio stabilizes in data-dominated regimes. This reflects the fact that both fluctuations are driven by uncertainty in a low-dimensional effective singular direction. In contrast, gauge-symmetric and piecewise-singular models exhibit pronounced decoupling. In these cases, $\hat{\nu}_{\text{thermo}}$ remains large due to persistent log-likelihood degeneracy, while $\hat{\nu}_{\text{geom}}$ collapses as the posterior concentrates along identifiable directions. As a result, the ratio $\hat{\nu}_{\text{geom}}/\hat{\nu}_{\text{thermo}}$ approaches zero even at moderate temperatures.

Sample-size dependence. Figure 18 shows the same ratios as a function of sample size n . Across all models, the ratio $\hat{\nu}_{\text{geom}}/\hat{\nu}_{\text{thermo}}$ stabilizes rapidly as n increases, converging to model-specific constants rather than to unity. This confirms that the observed discrepancies are not finite-sample artifacts, but reflect intrinsic differences between geometric and thermodynamic notions of fluctuation.

Trajectory interpretation. Joint trajectories in $(\hat{\nu}_{\text{thermo}}, \hat{\nu}_{\text{geom}})$ space reveal that agreement between the two quantities occurs only in effectively regular directions. In singular regimes, temperature changes induce curved, regime-dependent paths. This highlights that thermodynamic singular fluctuation captures global posterior softness that persists even when geometric variance collapses.

Experiment 7: Geometric vs Thermodynamic \check{v} Comparison (β -scan)

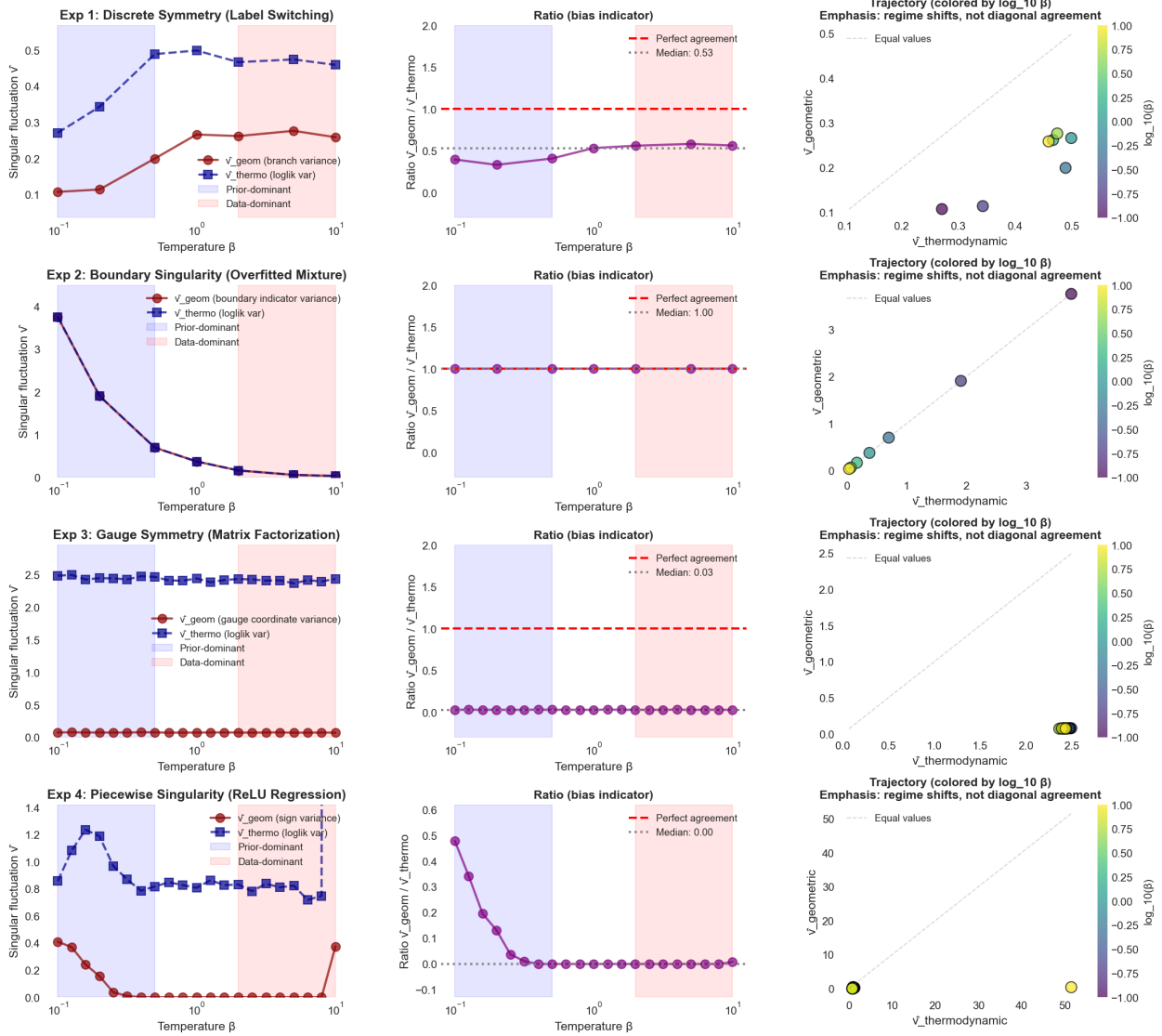


Figure 17: Experiment 7: Geometric vs. thermodynamic singular fluctuation under temperature variation. Comparison of geometric fluctuation estimates and thermodynamic singular fluctuation across inverse temperature β for four canonical singular models. **Left:** absolute values of \check{v}_{geom} and $\check{v}_{\text{thermo}}$. **Middle:** ratio $\check{v}_{\text{geom}} / \check{v}_{\text{thermo}}$, highlighting systematic deviations from unity. **Right:** joint trajectories in $(\check{v}_{\text{thermo}}, \check{v}_{\text{geom}})$ space, colored by $\log \beta$, emphasizing regime-dependent shifts rather than diagonal agreement.

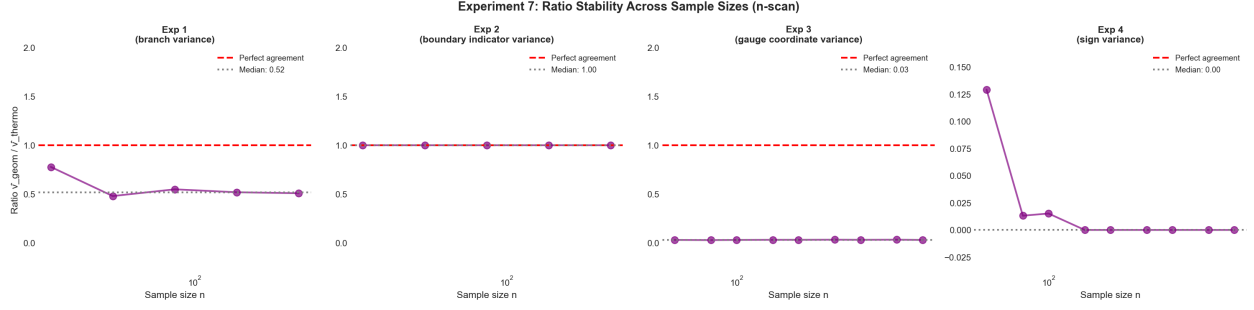


Figure 18: **Stability of geometric-to-thermodynamic fluctuation ratios with sample size.** Ratio $\hat{\nu}_{\text{geom}}/\hat{\nu}_{\text{thermo}}$ as a function of sample size n for the same four models. Ratios converge rapidly to model-specific limits, demonstrating that the two notions of singular fluctuation encode distinct aspects of posterior geometry.

Takeaway. Experiment 7 demonstrates that thermodynamic singular fluctuation is not merely a geometric proxy. Instead, it encodes global posterior sensitivity that can remain large even when local, symmetry-aligned geometric variance vanishes. This distinction is essential for understanding generalization, validating the equation of state, and characterizing singular learning behavior beyond local curvature.

5.9 Experiment 9: Estimator Comparison — WAIC vs. Thermodynamic Singular Fluctuation

This experiment compares two estimators of effective model complexity that originate from different perspectives: the Widely Applicable Information Criterion (WAIC) [Watanabe, 2010, 2013], widely used in Bayesian model assessment, and the thermodynamic singular fluctuation $\hat{\nu}_{\text{loglik}}$ introduced in Section 3.2. The purpose of this experiment is to empirically verify their theoretical equivalence in singular models and to situate WAIC within the thermodynamic framework developed throughout the paper.

Conceptual background. WAIC estimates effective complexity via posterior variance of pointwise log-likelihoods,

$$p_{\text{WAIC}} = \sum_{i=1}^n \text{Var}_{p(\theta|D)}[\log p(y_i | \theta)],$$

leading to a generalization-gap approximation p_{WAIC}/n . In singular learning theory, Watanabe showed that the same variance structure governs the second-order correction to the Bayesian free energy. At inverse temperature $\beta = 1$, this correction is quantified by the singular fluctuation ν , yielding the identity

$$p_{\text{WAIC}} = 2\nu.$$

From a thermodynamic perspective, WAIC therefore corresponds to a specific heat: a response coefficient measuring sensitivity of the posterior free energy to temperature perturbations.

Experimental setup. We evaluate this relationship across three representative singular models: (i) discrete symmetry via label switching, (ii) boundary singularity in an overfitted Gaussian mixture, and (iii) a piecewise singular ReLU regression model used as a stress test. For each model and a range of sample sizes n , we compute:

- p_{WAIC} from posterior log-likelihood samples,
- $\hat{\nu}_{\text{loglik}}$ using the functional variance estimator,
- the corresponding generalization-gap predictions p_{WAIC}/n and $2\hat{\nu}_{\text{loglik}}/n$.

All quantities are estimated from the same posterior samples; no test data or oracle information is used.

Estimator agreement. Figure 19 compares p_{WAIC} and $2\hat{\nu}_{\text{loglik}}$ directly. Across all models and sample sizes, the two estimates track each other closely. The ratio $p_{\text{WAIC}}/(2\hat{\nu}_{\text{loglik}})$ remains tightly concentrated around 1, indicating agreement up to small finite-sample effects. This holds even in the ReLU stress test, where posterior geometry is highly non-smooth and other asymptotic approximations degrade.

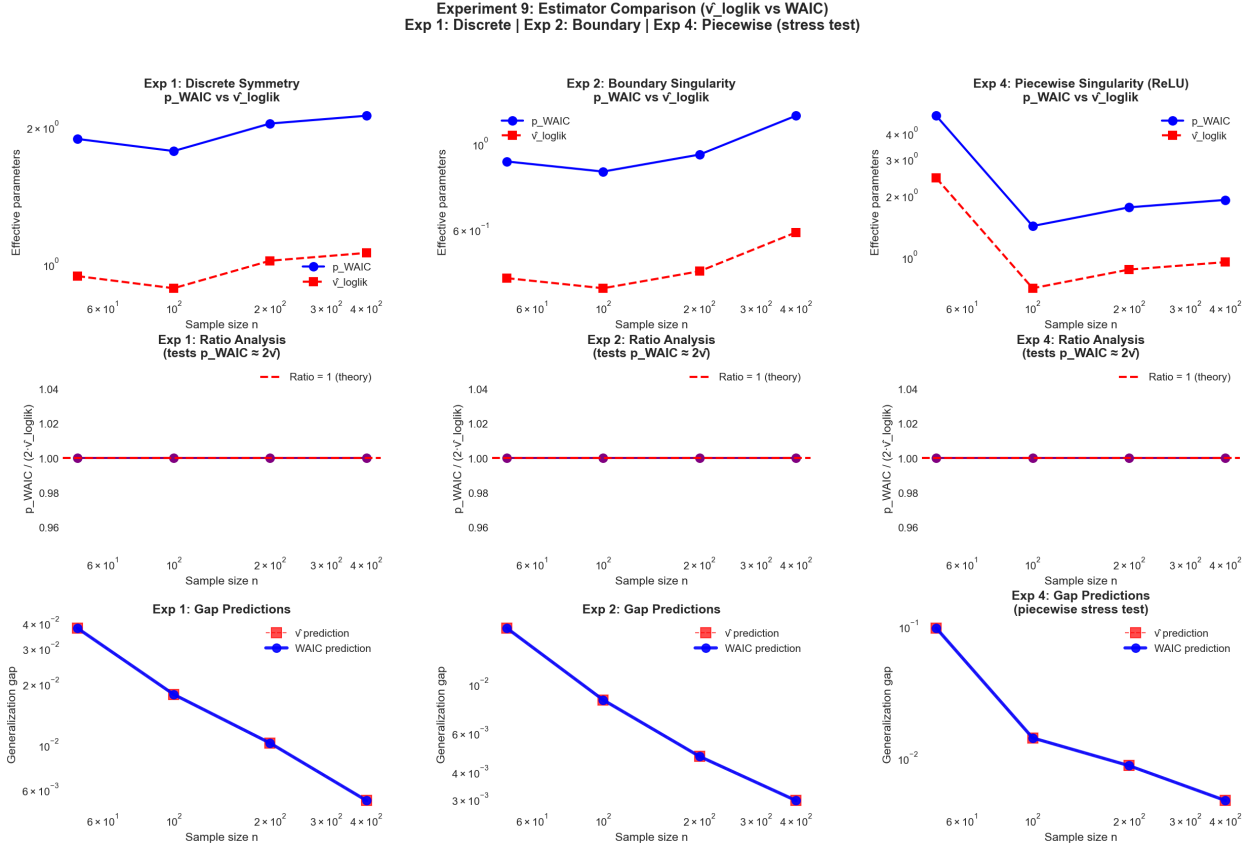


Figure 19: **Experiment 9: WAIC vs. thermodynamic singular fluctuation.** Comparison of effective complexity and generalization-gap estimators across three singular models: Exp. 1 (discrete symmetry), Exp. 2 (boundary singularity), and Exp. 4 (piecewise ReLU stress test). **Top row:** effective complexity estimates p_{WAIC} and $2\hat{\nu}_{\text{loglik}}$ as functions of sample size n . **Middle row:** ratio $p_{\text{WAIC}}/(2\hat{\nu}_{\text{loglik}})$ (theoretical target = 1), showing tight agreement across models and n . **Bottom row:** corresponding generalization-gap predictions p_{WAIC}/n and $2\hat{\nu}_{\text{loglik}}/n$, which are numerically indistinguishable. Agreement persists even in the piecewise ReLU model, confirming the identity $p_{\text{WAIC}} = 2\hat{\nu}_{\text{loglik}}$ at $\beta = 1$.

Generalization-gap predictions. The bottom row of Figure 19 shows the implied generalization-gap predictions. Predictions based on WAIC and on $\hat{\nu}_{\text{loglik}}$ are numerically indistinguishable across all settings considered. This confirms that the thermodynamic equation of state recovers classical generalization estimates when evaluated at $\beta = 1$.

Interpretation. Experiment 9 provides a direct empirical confirmation that WAIC is not an ad hoc correction but a special case of a thermodynamic response function. From this viewpoint, p_{WAIC} measures the number of effective predictive degrees of freedom, that is directions in parameter space along which posterior uncertainty induces variability in the predictive log-likelihood, that remain active under posterior uncertainty. Purely non-identifiable (gauge) directions, despite potentially large posterior variance, do not contribute. The thermodynamic formulation extends this interpretation beyond $\beta = 1$, allowing one to study temperature trajectories, phase transitions, and out-of-equilibrium behavior explored in earlier experiments.

Takeaway. WAIC coincides with twice the thermodynamic singular fluctuation in singular models, validating the statistical-physics interpretation of Bayesian generalization. This experiment anchors the thermodynamic framework to a familiar estimator, while clarifying that $\hat{\nu}$ provides strictly richer information once temperature dependence and regime structure are taken into account. These results also clarify a long-standing puzzle surrounding WAIC in singular models. Although geometric or manifold dimension is ill-defined in the presence of non-identifiability, WAIC remains well behaved because it does not estimate geometric dimension at all. Instead, it measures the variance of the log-likelihood under the posterior, which we identify as a thermodynamic response function. When the posterior is multimodal or supported on a lower-dimensional manifold, this variance aggregates predictive fluctuations across symmetry-related modes, boundary strata, or active-set transitions, while remaining insensitive to flat directions that do not affect predictions. From this perspective, WAIC continues to work in singular models precisely because it tracks posterior energy fluctuations rather than local geometric dimension.

5.10 Experiment 10: Symmetry Resolution in Multi-Unit ReLU Models

Role and singular mechanism. This experiment examines how singular fluctuations behave in a *multi-unit* neural network, where multiple symmetry mechanisms coexist and are resolved at different statistical rates. Unlike earlier experiments that probe temperature dependence or external-field responses, this experiment isolates the effect of increasing sample size, revealing how data progressively sharpens posterior geometry by breaking distinct symmetry directions. The goal is to contrast the behavior of thermodynamic and geometric notions of singular fluctuation as internal symmetries are resolved.

Model and setup. We consider a one-hidden-layer ReLU regression model with multiple exchangeable hidden units. This architecture exhibits two qualitatively distinct sources of non-identifiability: (i) *sign symmetries*, arising from ReLU invariance under coordinated sign flips and output scaling, and (ii) *permutation symmetries*, corresponding to relabelings of hidden units. Both induce singular posterior geometry at small sample sizes.

All diagnostics are evaluated at inverse temperature $\beta = 1$, isolating the data-dominated regime. For each sample size n , we compute:

- the thermodynamic singular fluctuation $\hat{\nu}_{\text{loglik}}$ from posterior log-likelihood variance;

- a geometric singular fluctuation $\hat{\nu}_{\text{geom}}$, decomposed into sign- and permutation-related components;
- entropies of sign configurations and unit permutations;
- variance decompositions associated with each symmetry mode;
- unit death rates, defined as the posterior probability that a unit's weight norm falls below a fixed threshold.

Experiment 10: Multi-Unit ReLU - Sample Size Scan

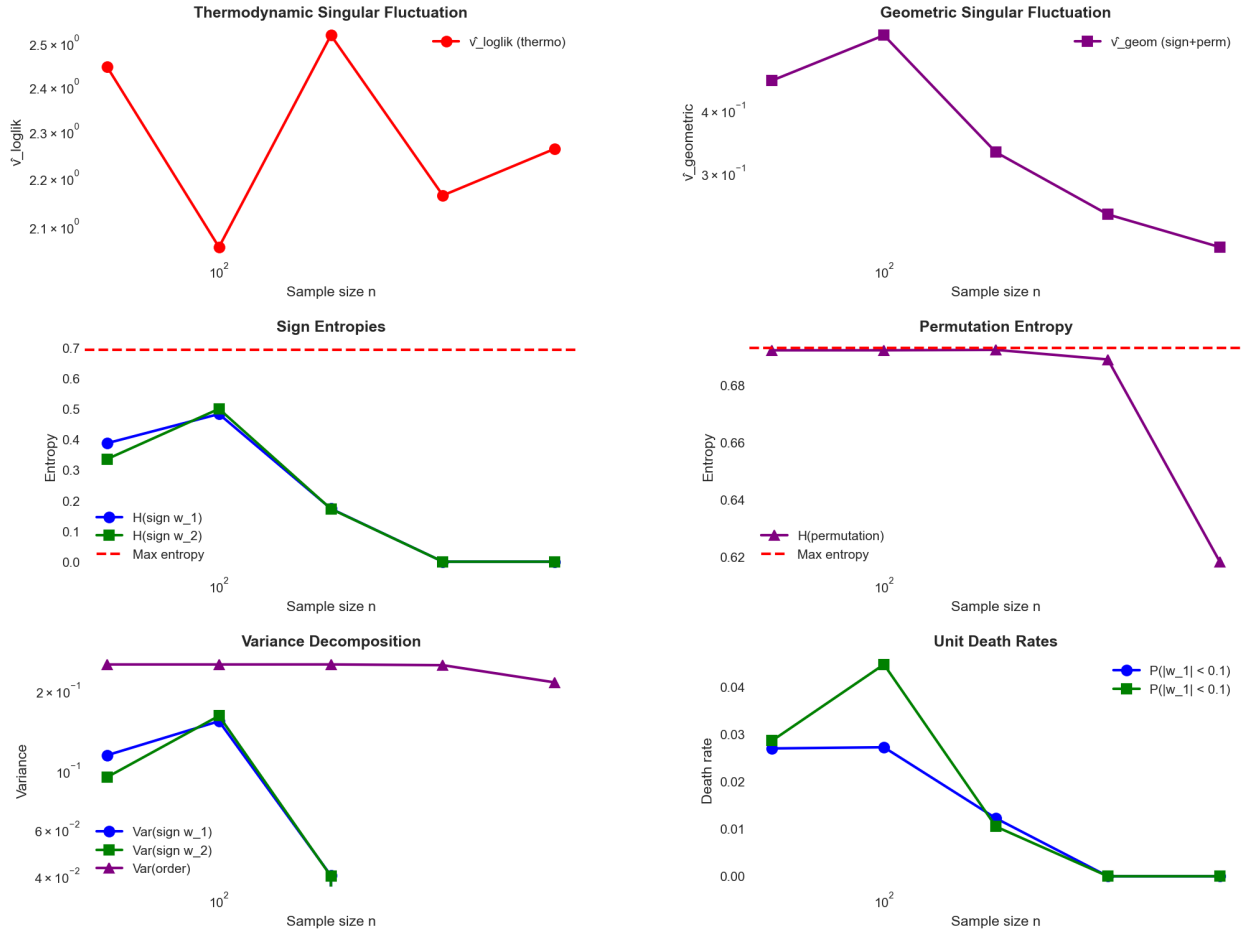


Figure 20: **Experiment 10: Multi-unit ReLU regression (sample-size scan).** Thermodynamic and geometric singular fluctuations, entropy diagnostics, variance decompositions, and unit death rates as functions of sample size. Thermodynamic fluctuation remains large across n , while geometric fluctuation decays as internal symmetries are progressively resolved.

Thermodynamic versus geometric fluctuation. Figure 20 (top row) shows a clear divergence between thermodynamic and geometric behavior. The thermodynamic singular fluctuation $\hat{\nu}_{\text{loglik}}$ remains large and weakly dependent on n , reflecting persistent global posterior softness. In contrast,

the geometric fluctuation $\hat{\nu}_{\text{geom}}$ decreases monotonically with sample size, indicating that identifiable symmetry directions are progressively resolved by data.

Entropy collapse and symmetry resolution. Entropy diagnostics reveal a separation of symmetry-breaking timescales. Sign entropy collapses rapidly as n increases, showing that the posterior quickly commits to a consistent sign configuration. Permutation entropy, however, remains near its maximum over a much wider range of sample sizes before eventually decreasing. This confirms that permutation symmetries are statistically harder to resolve than sign symmetries, despite both contributing to singular geometry at small n .

Variance decomposition and unit death. Variance decompositions show that the decay of geometric singular fluctuation is driven primarily by the collapse of sign-related variance, while permutation-related variance persists longer. Importantly, this effect is *not* explained by unit death: the probability that a unit’s weight norm collapses decreases with increasing n , indicating that symmetry resolution occurs through posterior concentration rather than degenerate pruning of units.

Takeaway. Experiment 10 demonstrates that in realistic, overparameterized neural models, different singular directions are resolved at different statistical rates. Geometric singular fluctuation decomposes and vanishes as symmetries are broken, while thermodynamic singular fluctuation remains sensitive to global posterior uncertainty. This separation explains why thermodynamic fluctuation remains essential for generalization analysis even after geometric symmetries are resolved. This experiment demonstrates that thermodynamic singular fluctuation remains the relevant quantity for generalization even after geometric symmetries are resolved.

6 Thermodynamic Structure of Singular Bayesian Models

We now connect the thermodynamic formulation of singular learning developed above to the widely used Widely Applicable Information Criterion (WAIC). This section shows that WAIC is not an ad hoc correction for singular models, but rather a special case of a thermodynamic response function measuring posterior fluctuations of the log-likelihood. From this perspective, the effective degrees of freedom estimated by WAIC should be understood in a predictive rather than geometric sense: they correspond to directions in parameter space along which posterior uncertainty induces variability in predictions, not to local manifold dimension. This interpretation explains why WAIC remains well behaved in the presence of non-identifiability, multimodality, and stratified parameter spaces. Moreover, the thermodynamic framework extends this connection beyond the standard posterior ($\beta = 1$), enabling the study of temperature dependence, regime structure, and phase behavior that are invisible to classical information criteria.

6.1 Singular fluctuation as persistent uncertainty along non-identifiable directions

A central message of this work is that the *singular fluctuation* ν should not be interpreted merely as a correction term in asymptotic generalization formulas, but rather as a quantitative summary of *persistent posterior uncertainty along non-identifiable directions of the model*. This interpretation emerges consistently across all singular structures examined in Experiments 1–4.

In regular models, posterior contraction occurs uniformly in all parameter directions, and fluctuations vanish at the standard $n^{-1/2}$ rate. In contrast, singular models contain directions, which arise from symmetries, gauge freedoms, or active-set degeneracies, along which the likelihood is locally flat or only weakly informative. Along these directions, posterior uncertainty decays slowly, or may persist over wide ranges of sample size n or inverse temperature β . Our experiments demonstrate that $\hat{\nu}$ systematically tracks this phenomenon:

- In discrete symmetry models (Experiments 1 and 4), $\hat{\nu}$ is large precisely when the posterior mixes between symmetry-related branches and decreases as symmetry is broken.
- In continuous gauge models (Experiment 3), $\hat{\nu}$ reflects the gradual narrowing of posterior mass along a non-identifiable gauge orbit.
- In over-parameterized mixture models (Experiment 2), $\hat{\nu}$ remains elevated when redundant components remain weakly constrained.

Across all cases, $\hat{\nu}$ behaves as a *model-level measure of unresolved ambiguity*, rather than a parameter-wise variance. Importantly, this ambiguity is structural: it is tied to the geometry of the likelihood and persists even when identifiable functions of the parameters are well estimated. This perspective clarifies why singular fluctuation appears in learning curves and information criteria: it quantifies how much freedom the posterior retains to move along singular strata, even as prediction error decreases.

Key takeaway. Singular fluctuation measures the extent to which learning remains incomplete due to non-identifiability, rather than lack of data.

6.2 Entropy flow and symmetry occupancy

The behavior of $\hat{\nu}$ can be further understood through the lens of *entropy flow* and *symmetry occupancy*. Singular learning is not characterized by a single static entropy level, but by how posterior mass redistributes across symmetry-related regions as learning proceeds.

Let \mathcal{S} denote a symmetry set (e.g., sign branches, permutation orbits, gauge manifolds). We may associate to the posterior a distribution over \mathcal{S} , whose entropy reflects how broadly the posterior occupies these equivalent representations. Our experiments reveal a common pattern:

1. At small n or low β , posterior mass is broadly distributed across \mathcal{S} , leading to high symmetry entropy.
2. As n or β increases, mass concentrates unevenly, inducing entropy flow as occupancy shifts.
3. Eventually, entropy collapses (discrete symmetries) or narrows (continuous symmetries), signaling effective symmetry breaking.

Crucially, singular fluctuation does *not* peak at maximal entropy, but rather during periods of *rapid entropy change*. In Experiments 1 and 4, $\hat{\nu}$ is largest when the posterior transitions from symmetric mixing to asymmetric concentration. In Experiment 3, $\hat{\nu}$ decreases smoothly as gauge occupancy narrows, reflecting gradual entropy flow rather than abrupt collapse. This behavior mirrors the role of specific heat in statistical physics, where fluctuations peak at points of maximal sensitivity rather than maximal disorder [Pathria and Beale, 2021]. Here, $\hat{\nu}$ detects when the posterior is most responsive to small changes in data or temperature, corresponding to active redistribution of mass along singular manifolds.

Key takeaway. Singular fluctuation tracks the *dynamics of posterior reallocation across symmetry sets*, not merely their size or entropy.

6.3 Geometric versus thermodynamic notions of fluctuation

A recurring theme in our analysis is the distinction between two complementary notions of fluctuation, both of which are naturally referred to as “singular fluctuation” but serve different roles.

Geometric fluctuation. In several experiments, we introduced geometric estimators of ν based on variance along explicitly identified non-identifiable coordinates:

- Sign indicators in piecewise or symmetric models (Experiments 1 and 4).
- Gauge coordinates in matrix factorization (Experiment 3).

These quantities directly measure posterior spread along singular directions and provide clear geometric intuition. They are particularly useful for diagnosing the structure and dimensionality of singular strata.

Thermodynamic fluctuation. In contrast, the thermodynamic definition of ν arises from log-likelihood fluctuations,

$$\nu = \frac{\beta}{2} \sum_{i=1}^n \text{Var}[\log p(y_i | w)],$$

and governs the equation-of-state relationship

$$\hat{G} - \hat{T} \approx \frac{2\nu}{n}.$$

This quantity is invariant to reparameterization and is the correct object for generalization analysis and information criteria. Our experiments show that these two notions are closely related but not identical. Geometric fluctuations explain *why* thermodynamic fluctuation is large: unresolved motion along singular directions induces variability in predictive likelihoods. However, only the thermodynamic ν satisfies universal identities linking training and generalization error. This distinction resolves apparent inconsistencies observed in Experiment 3, where gauge variance persisted while the equation-of-state relation required a different estimator. Rather than a contradiction, this reflects the fact that geometry diagnoses *where* uncertainty lives, while thermodynamics governs *how it affects prediction*.

Key takeaway. Geometric and thermodynamic fluctuations are complementary: the former reveals the structure of singular uncertainty, while the latter determines its statistical consequences.

7 Discussion and Future Work

This work revisits singular learning theory from a finite-temperature, statistical-physics perspective, with the goal of clarifying what the *singular fluctuation* ν reveals about the geometry and dynamics of singular statistical models. By interpreting ν as an analog of specific heat, and by introducing additional response quantities such as prior susceptibility and entropy-based diagnostics, we obtain a more operational and geometric understanding of singular models beyond asymptotic learning curves. We conclude by outlining several theoretical, methodological, and practical directions opened by this viewpoint.

7.1 Theoretical directions

A natural extension of this work is toward a more complete *finite-sample theory* of singular learning. Classical SLT focuses on asymptotic expansions of the marginal likelihood and generalization error as $n \rightarrow \infty$, characterized by invariants such as the real log canonical threshold (RLCT) and singular fluctuation. Our results suggest that finite-temperature quantities such as $\nu(\beta, n)$, susceptibilities, and entropy flows encode meaningful information well before the asymptotic regime. Developing non-asymptotic bounds or concentration results for these quantities would help bridge SLT with modern learning-theoretic analyses.

From a modeling perspective, many important singularities remain unexplored. Higher-rank matrix factorizations introduce multi-dimensional gauge manifolds, leading to richer symmetry structures and potentially multiple interacting “soft modes.” Similarly, deep neural networks exhibit layered rescaling symmetries, activation-induced piecewise singularities, and parameter redundancies whose combined effects are poorly understood. Extending the present analysis to multi-layer ReLU networks or other modern architectures would clarify how singular fluctuations accumulate or interact across layers.

At a more speculative level, the thermodynamic formulation suggests connections to field-theoretic tools. The appearance of continuous gauge directions, entropy flows, and response functions hints at an effective low-energy description of learning dynamics near singular strata. Exploring whether renormalization, effective actions, or other techniques from statistical field theory can be meaningfully adapted to singular learning remains an open and intriguing direction.

7.2 Methodological and practical directions

Beyond theory, the quantities studied here admit practical interpretations as *diagnostics* for Bayesian learning systems. Singular fluctuation ν quantifies residual uncertainty along non-identifiable or weakly identifiable directions, while prior susceptibility χ_π measures sensitivity to regularization choices. These quantities can be estimated from posterior samples and do not require explicit knowledge of the model’s singularity structure.

This suggests several practical applications. For example, monitoring ν or entropy-based measures during training could help identify regimes of slow mixing, symmetry persistence, or incipient phase transitions. Susceptibility measures may serve as indicators of robustness or instability with respect to prior specification, complementing existing diagnostics such as effective sample size or posterior predictive checks. In variational inference, analogous quantities could potentially be used to detect when an approximation collapses singular structure prematurely.

Another promising direction is model comparison. While WAIC and WBIC provide scalar summaries, the thermodynamic quantities introduced here offer a richer, multi-dimensional characterization of model behavior. Comparing models based on their singular fluctuations, susceptibilities, or entropy profiles may reveal differences invisible at the level of predictive accuracy alone.

7.3 Limitations

The present study also has several limitations. First, the experimental models are deliberately small and stylized in order to isolate specific types of singularities. While this is appropriate for conceptual clarity, scaling these ideas to large, high-dimensional models will require further algorithmic and computational advances. In particular, MCMC-based estimation of thermodynamic quantities can be computationally expensive, and careful variance reduction or approximation techniques will be needed in practice.

Second, our analysis focuses primarily on posterior geometry and equilibrium properties. We do not directly address optimization dynamics, transient behavior, or algorithm-dependent effects, all of which play a central role in modern deep learning. Understanding how singular fluctuations and susceptibilities interact with optimization algorithms remains an important open problem.

Finally, while the statistical physics analogies used here are powerful, they should be interpreted with care. Our goal is not to claim a literal physical correspondence, but rather to use the language and tools of statistical mechanics as a guide for organizing and interpreting complex statistical phenomena. Clarifying the precise scope and limits of these analogies is itself an important direction for future work.

Variational inference and renormalization of singular geometry. A major limitation of the present work is that all thermodynamic quantities are defined with respect to the exact Bayesian posterior, which in singular models is typically accessible only through costly MCMC-based schemes. In many modern applications, including deep networks, large mixture models, and hierarchical latent-variable models, exact posterior sampling is infeasible, and inference is performed using variational approximations.

It is well known that variational inference can fundamentally alter the singular structure of a model [Watanabe, 2018, Yang et al., 2020, Zhang et al., 2017]. In particular, the real log canonical threshold (RLCT) generally changes under variational restrictions, reflecting the fact that variational families break symmetries, collapse non-identifiable directions, and induce artificial identifiability [Nakajima et al., 2019]. From the thermodynamic perspective developed here, this implies that both the singular fluctuation ν and related response functions are *renormalized* by the variational approximation.

Understanding how variational inference modifies entropy, entropy flow, and singular fluctuation is therefore an important direction for future work. A central open question is whether variational posteriors admit effective thermodynamic descriptions, with well-defined analogues of specific heat and phase transitions, and how these quantities relate to their exact Bayesian counterparts. Such a theory would provide principled diagnostics for variational approximations in singular models, beyond traditional ELBO-based criteria.

Outlook. Overall, we view singular fluctuation not merely as an asymptotic correction term, but as a finite-temperature descriptor of how singular structure remains active during learning. By combining geometric insight with thermodynamic intuition, we hope this work provides a foundation for more interpretable and diagnostically useful theories of singular statistical models.

8 Conclusion

This paper develops a thermodynamic perspective on singular Bayesian learning, with singular fluctuation at its core. By interpreting ν as the specific heat of the posterior, we provide a clear and operational answer to a long-standing open question in singular learning theory: what singular fluctuation *means* statistically.

Across a wide range of models and experiments, a consistent picture emerges. Singular fluctuation measures persistent posterior softness along non-identifiable directions, which may arise from discrete symmetries, boundary strata, continuous gauge freedoms, or piecewise activation patterns. Unlike local curvature or parameter variance, ν captures global fluctuations of the log-likelihood and governs universal identities linking training error, generalization error, and free energy.

The thermodynamic framework developed here goes beyond ν alone. Entropy flow reveals when and how posterior mass redistributes across singular regions. Prior and cross-susceptibilities quantify the extent to which regularization shapes learning along weakly identified directions. Active-set entropy distinguishes discrete symmetry mixing from continuous degeneracy. Together, these quantities form a coordinated diagnostic suite that exposes the geometry of learning in singular models.

Our experiments demonstrate that these thermodynamic signatures are remarkably robust. They distinguish fundamentally different singularity types, remain informative at finite sample sizes, and align naturally with classical quantities such as WAIC. In particular, the empirical equivalence $p_{\text{WAIC}} = 2\nu$ anchors the thermodynamic interpretation in familiar statistical practice, while extending it to temperature scans, phase-transition behavior, and geometric diagnostics unavailable to WAIC alone.

Looking forward, the thermodynamic viewpoint suggests several promising directions. Most importantly, it highlights the need to understand how approximate inference methods, especially variational inference, renormalize singular geometry. Since variational families often break symmetries and collapse non-identifiable directions, they necessarily alter specific heat, entropy flow, and susceptibilities. Developing a thermodynamic theory of approximate posteriors may provide principled diagnostics for approximation bias in singular models.

More broadly, we view singular learning not as a pathological corner case, but as the generic setting for modern statistical models. By importing the language and tools of statistical mechanics in a precise and disciplined way, we gain a unifying framework for understanding uncertainty, generalization, and geometry in these models. We hope this work serves as a foundation for further connections between singular learning theory, Bayesian inference, and the thermodynamics of learning.

References

Pierre Alquier, James Ridgway, and Nicolas Chopin. On the properties of variational approximations of gibbs posteriors. *Journal of Machine Learning Research*, 17(236):1–41, 2016.

Shun-ichi Amari, Noboru Murata, Klaus-Robert Müller, Michael Finke, and Howard Yang. Statistical theory of overtraining-is cross-validation asymptotically effective? *Advances in neural information processing systems*, 8, 1995.

Shun-ichi Amari, Noboru Murata, K-R Muller, Michael Finke, and Howard Hua Yang. Asymptotic statistical theory of overtraining and cross-validation. *IEEE transactions on neural networks*, 8 (5):985–996, 1997.

Monica Bianchini and Franco Scarselli. On the complexity of neural network classifiers: A comparison between shallow and deep architectures. *IEEE transactions on neural networks and learning systems*, 25(8):1553–1565, 2014.

Ariel Caticha and Roland Preuss. Maximum entropy and bayesian data analysis: Entropic prior distributions. *Physical Review E—Statistical, Nonlinear, and Soft Matter Physics*, 70(4):046127, 2004.

Olivier Catoni. *Statistical learning theory and stochastic optimization: Ecole d’Eté de Probabilités de Saint-Flour XXXI-2001*. Springer, 2004.

Pratik Chaudhari, Anna Choromanska, Stefano Soatto, Yann LeCun, Carlo Baldassi, Christian Borgs, Jennifer Chayes, Levent Sagun, and Riccardo Zecchina. Entropy-sgd: Biasing gradient descent into wide valleys. *Journal of Statistical Mechanics: Theory and Experiment*, 2019(12):124018, 2019.

Anna Choromanska, Mikael Henaff, Michael Mathieu, Gérard Ben Arous, and Yann LeCun. The loss surfaces of multilayer networks. In *Artificial intelligence and statistics*, pages 192–204. PMLR, 2015.

Yann N Dauphin, Razvan Pascanu, Caglar Gulcehre, Kyunghyun Cho, Surya Ganguli, and Yoshua Bengio. Identifying and attacking the saddle point problem in high-dimensional non-convex optimization. *Advances in neural information processing systems*, 27, 2014.

J. K. Ghosh, M. Delampady, and T. Samanta. *An Introduction to Bayesian Analysis: Theory and Methods*. Springer, 2006.

Ryan Giordano, Tamara Broderick, and Michael I Jordan. Covariances, robustness, and variational bayes. *Journal of machine learning research*, 19(51):1–49, 2018.

Peter Grünwald. The safe bayesian: learning the learning rate via the mixability gap. In *International Conference on Algorithmic Learning Theory*, pages 169–183. Springer, 2012.

Paul Gustafson. *Measurement Error and Misclassification in Statistics and Epidemiology*. Chapman & Hall/CRC, 2001.

Bas JK Kleijn and Aad W Van der Vaart. The bernstein-von-mises theorem under misspecification. 2012.

David JC MacKay. *Information theory, inference and learning algorithms*. Cambridge university press, 2003.

Marc Mezard and Andrea Montanari. *Information, physics, and computation*. Oxford University Press, 2009.

Shinichi Nakajima, Kazuho Watanabe, and Masashi Sugiyama. *Variational Bayesian learning theory*. Cambridge University Press, 2019.

Radford M. Neal. *Bayesian Learning for Neural Networks*, volume 118 of *Lecture Notes in Statistics*. Springer, 1996.

Manfred Opper and David Saad. *Advanced mean field methods: Theory and practice*. MIT press, 2001.

R.K. Pathria and P.D. Beale. *Statistical Mechanics*. Academic Press, 2021.

Judith Rousseau and Kerrie Mengersen. Asymptotic behaviour of the posterior distribution in overfitted mixture models. *Journal of the Royal Statistical Society Series B: Statistical Methodology*, 73(5):689–710, 2011.

Levent Sagun, Utku Evci, V Ugur Guney, Yann Dauphin, and Leon Bottou. Empirical analysis of the hessian of over-parametrized neural networks. *arXiv preprint arXiv:1706.04454*, 2017.

Nathan Srebro and Adi Shraibman. Rank, trace-norm and max-norm. In *International conference on computational learning theory*, pages 545–560. Springer, 2005.

Alexandre B Tsybakov. *Introduction to Nonparametric Estimation*. Springer, 2008.

Sumio Watanabe. *Algebraic Geometry and Statistical Learning Theory*. Cambridge University Press, 2009.

Sumio Watanabe. Asymptotic equivalence of bayes cross validation and widely applicable information criterion in singular learning theory. *Journal of Machine Learning Research*, 11:3571–3594, 2010.

Sumio Watanabe. A widely applicable bayesian information criterion. *The Journal of Machine Learning Research*, 14(1):867–897, 2013.

Sumio Watanabe. *Mathematical Theory of Bayesian Statistics*. CRC Press, 2018.

Sumio Watanabe. Recent advances in algebraic geometry and bayesian statistics. *Information Geometry*, 7(Suppl 1):187–209, 2024.

Yun Yang, Debdeep Pati, and Anirban Bhattacharya. α -variational inference with statistical guarantees. *The Annals of Statistics*, 48(2):886–905, 2020.

Cheng Zhang, Judith Butepage, Hedvig Kjellstrom, and Stephan Mandt. Noisy natural gradient as variational inference. *Proceedings of the 34th International Conference on Machine Learning*, 2017.

A Thermodynamic Identities and Estimators

This appendix collects technical definitions and derivations underlying the thermodynamic diagnostics used throughout the experiments. The purpose is to make the estimators reproducible and to clarify the assumptions under which the equation-of-state (EOS) relations hold.

A.1 Free energy, generalization, and temperature

Let $p(y | w)$ denote the likelihood and $\pi(w)$ a prior over parameters $w \in \mathcal{W}$. For inverse temperature β , the tempered posterior is

$$p_\beta(w | D) \propto \pi(w) \exp(-\beta n \ell(w)), \quad \ell(w) = -\frac{1}{n} \log p(D | w).$$

The (empirical) free energy is defined as

$$F_n(\beta) = -\frac{1}{\beta n} \log \int \pi(w) \exp(-\beta n \ell(w)) dw.$$

Thermodynamic quantities are obtained as derivatives of $\beta F_n(\beta)$. In particular, we define

$$\hat{G}(\beta) = \frac{\partial}{\partial \beta} (\beta F_n(\beta)), \quad \hat{T}(\beta) = \mathbb{E}_{p_\beta}[\ell(w)],$$

which correspond, respectively, to generalization and training observables in the statistical mechanics analogy.

A.2 Singular fluctuation and equation of state

The thermodynamic singular fluctuation $\hat{\nu}$ is defined as

$$\hat{\nu} = \frac{n}{2} (\hat{G} - \hat{T}),$$

motivated by Watanabe's equation-of-state for singular models. In regular models, $\hat{\nu}$ converges to the parameter dimension, while in singular models it encodes effective complexity determined by local geometry.

In practice, we estimate $\hat{\nu}$ using the empirical EOS relation

$$\hat{G} - \hat{T} \approx \frac{2\hat{\nu}}{n}, \tag{14}$$

which holds asymptotically under mild regularity conditions. Throughout the experiments, this relation is used diagnostically rather than as a strict identity.

Validity and failure modes. Equation (14) is exact in regular models and asymptotically valid for many singular models. Deviations may occur: (i) at small sample sizes, (ii) near boundary singularities where posterior mass accumulates at the edge of parameter space, or (iii) in piecewise models where likelihood curvature is discontinuous. We report EOS residuals explicitly when relevant.

A.3 Estimators of singular fluctuation

We use two complementary estimators of $\hat{\nu}$.

Global (thermodynamic) estimator. The primary estimator is obtained directly from the EOS:

$$\hat{\nu}_{\text{EOS}} = \frac{n}{2}(\hat{G} - \hat{T}),$$

where \hat{G} and \hat{T} are computed via Monte Carlo averages under $p_\beta(w \mid D)$.

Functional (variance-based) estimator. For an observable $\phi(w)$, linear-response theory predicts

$$\frac{d}{dh} \mathbb{E}_{\pi_h}[\phi] \Big|_{h=0} = \text{Var}_{p_\beta}(\phi),$$

where $\pi_h(w) \propto \pi(w) \exp(h\phi(w))$. When ϕ probes identifiable directions of the likelihood, the resulting variance provides an alternative estimator of singular fluctuation. Agreement between global and functional estimators is used as a consistency check.

A.4 Susceptibilities

We define the prior susceptibility associated with an observable ϕ as

$$\chi_\pi(\phi) = \text{Var}_{p_\beta}(\phi),$$

interpreted as the linear response of posterior expectations to small prior perturbations. Cross-susceptibilities involving temperature are defined analogously via mixed derivatives of $\beta F_n(\beta)$. These quantities are used to diagnose sensitivity rather than generalization.